

Fully time-dependent cloud formation from a non-equilibrium gas-phase in exoplanetary atmospheres

S. Kiefer^{1,2,3}, H. Lecoq-Molinos^{2,3,1}, Ch. Helling^{2,3}, N. Bangera^{2,3}, and L. Decin¹

¹ Institute of Astronomy, KU Leuven, Celestijnenlaan 200D, 3001 Leuven, Belgium
e-mail: sven.kiefer@kuleuven.be

² Space Research Institute, Austrian Academy of Sciences, Schmiedlstrasse 6, A-8042 Graz, Austria

³ Institute for Theoretical Physics and Computational Physics, Graz University of Technology, Petersgasse 16 8010 Graz

Received ...; accepted ...

ABSTRACT

Context. Recent observations suggest the presence of clouds in exoplanet atmospheres but have also shown that certain chemical species in the upper atmosphere might not be in chemical equilibrium. Present and future interpretation of data from, for example, CHEOPS, JWST, PLATO and Ariel requires a combined understanding of the gas-phase and the cloud chemistry.

Aims. The goal of this work is to calculate the two main cloud formation processes, nucleation and bulk growth, consistently from a non-equilibrium gas-phase. The aim is further to explore the interaction between a kinetic gas-phase and cloud micro-physics.

Methods. The cloud formation is modelled using the moment method and kinetic nucleation which are coupled to a gas-phase kinetic rate network. Specifically, the formation of cloud condensation nuclei is derived from cluster rates that include the thermochemical data of $(\text{TiO}_2)_N$ from $N = 1$ to 15. The surface growth of 9 bulk Al/Fe/Mg/O/Si/S/Ti binding materials considers the respective gas-phase species through condensation and surface reactions as derived from kinetic disequilibrium. The effect of completeness of rate networks and the time evolution of the cloud particle formation is studied for an example exoplanet HD 209458 b.

Results. A consistent, fully time-dependent cloud formation model in chemical disequilibrium with respect to nucleation, bulk growth and the gas-phase is presented and first test cases are studied. This model shows that cloud formation in exoplanet atmospheres is a fast process. This confirms previous findings that the formation of cloud particles is a local process. Tests on selected locations within the atmosphere of the gas-giant HD 209458 b show that the cloud particle number density and volume reach constant values within 1s. The complex kinetic polymer nucleation of TiO_2 confirms results from classical nucleation models. The surface reactions of $\text{SiO}[s]$ and $\text{SiO}_2[s]$ can create a catalytic cycle that dissociates H_2 to 2 H, resulting in a reduction of the CH_4 number densities.

Key words. Astrochemistry – Planets and satellites: atmospheres – Methods: analytical

1. Introduction

Clouds and dust are present in many astrophysical environments. In stellar environments, dust can be found in the outflows of asymptotic giant branch (AGB) stars (e.g. Gail et al. 1984; Fleischer et al. 1999; Ferrarotti & Gail 2006; Höfner 2009; Gobrecht et al. 2016; Khouri et al. 2016; Decin et al. 2017) and Wolf–Rayet (WR) stars (Williams et al. 1987; Crowther 2003; Lau et al. 2022). It can also be found in supernova (Tinyanont et al. 2019; Niculescu-Duvaz et al. 2022; Zhang et al. 2022). Dust produced in these environments replenishes the interstellar medium (ISM) through radiation driven mass loss. In cooler objects, clouds are predicted within brown dwarfs (Allard et al. 2001; Ackerman & Marley 2001; Helling et al. 2004) and indirect evidence of clouds in brown dwarfs has been found (Maire et al. 2020; Ward-Duong et al. 2020; Kammerer et al. 2021). Exoplanet atmospheres are also expected to have a strong cloud presence (Helling et al. 2023). Cloud particles typically have large opacities which lead to characteristically flat spectra in the optical and near infrared. And indeed, several exoplanet observations in these wavelength ranges show a flat spectrum (Bean et al. 2010; Kreidberg et al. 2014; Espinoza et al. 2019; Spyrtos et al. 2021; Libby-Roberts et al. 2022). To understand cloud formation, one also needs to understand gas-phase chemistry and the nucleation process. In AGB stars, many chemical species have been detected (e.g. AlF, MgNC, NaCN, CO, SiO, HCN,

CS, PAHs; Highberger et al. 2001; Decin et al. 2008; Smolders et al. 2010). For exoplanets, recent medium and high resolution observations detected the presence of several atomic (e.g. Mg, Na, Ca, Cr, Fe, Ni, V, Ti, Mn, O; Hoeijmakers et al. 2018a, 2020; Prinoth et al. 2022; Borsa et al. 2022) and molecular species (e.g. CO, H_2O , CH_4 , NH_3 , C_2H_2 ; Kok et al. 2013; Hoeijmakers et al. 2018b; Guilluy et al. 2022; Guillot et al. 2022) pointing to a chemically rich environment.

In collisionally dominated environments, the gas-phase can be modeled using chemical equilibrium models (Stock et al. 2018; Woitke & Helling 2021). This is a good assumption for the deep atmosphere of exoplanets and brown dwarfs (Venot et al. 2018) where the collisional timescales become small. In low density environments, like the outflow of AGB stars (Plane & Robertson 2022; Sande & Millar 2019) and the upper atmospheres of exoplanets (Rimmer & Helling 2013; Baxter et al. 2021; Tsai et al. 2023; Mendonça et al. 2018) and brown dwarfs (Helling & Rimmer 2019; Lee et al. 2020), collisional timescales become large. In these environments, chemical disequilibrium processes, like radiation or quenching, can drive the gas-phase abundances out of equilibrium.

The formation of clouds and dust starts with the formation of cloud condensation nuclei (CCNs). In gaseous exoplanets, CCNs cannot originate from the planet’s surface, like in terrestrial planets, but have to be formed directly from the gas-phase through

nucleation, which marks the transition from gas-phase chemistry to solid-phase chemistry. Classical nucleation theory (CNT) or modified classical nucleation theory (MCNT) is an often used approach to describe the rate at which CCNs are formed (nucleation rate). In order to describe the actual formation of clusters leading up to CCNs, a kinetic description can be used. (Patzer et al. 1998; Lee et al. 2015; Bromley et al. 2016; Boulangier et al. 2019; Köhn et al. 2021; Gobrecht et al. 2022). To calculate kinetic nucleation, the thermodynamic properties of clusters of the nucleating species have to be known. There are active efforts to derive the structures and properties of species that are associated with nucleation processes (Chang et al. 2005, 2013; Patzer et al. 2014; Lee et al. 2015; Gobrecht et al. 2022; Sindel et al. 2022; Andersson et al. 2023). Even in the cases where data is available, it is often limited to the smallest cluster sizes because calculating the required properties becomes more computationally intensive for larger clusters (Sindel et al. 2022).

Supersaturated species can grow onto CCNs once they are present. There are two main ways these bulk growth processes can occur. Firstly there is condensation, which describes the deposition of gas-phase species onto CCNs (e.g. $\text{SiO} \rightarrow \text{SiO}[\text{s}]$). Many models use condensation curves to determine where clouds can form (e.g. Demory et al. 2013; Webber et al. 2015; Crossfield 2015; Kempton et al. 2017; Roman & Rauscher 2017; Roman et al. 2021). Secondly, bulk growth can occur through kinetic surface reactions (Patzer et al. 1998; Helling & Woitke 2006; Helling & Fomins 2013). In contrast to condensation, surface reactions include multiple chemical species to form the bulk material (e.g. $\text{SiS} + \text{H}_2\text{O} \rightarrow \text{SiO}[\text{s}] + \text{H}_2\text{S}$). In addition to providing additional bulk growth paths for condensing species, surface reactions also allow the bulk growth of materials which may not be stable in the gas-phase themselves. Both processes can be described kinetically (Patzer et al. 1998).

In this paper, we present a fully time-dependent description of the processes that lead to the formation of clouds in exoplanets, or dust in brown dwarfs, stars, and supernovae. We advance the nucleation description by modeling potential chemical pathways based on thermodynamic cluster properties and expand the kinetic description of surface reactions to chemical disequilibrium. With this model, we study the timescales of cloud formation in exoplanet atmospheres. The description of the chemical network, kinetic nucleation and bulk growth is given in Sect. 2. The kinetic chemistry and kinetic nucleation are investigated in Sect. 3. The fully kinetic cloud formation model is then applied to temperature-pressure ($T_{\text{gas}}-p_{\text{gas}}$) points within the atmosphere of HD 209458 b (Sect. 4). Lastly, the summary is given in Sect. 5.

2. Model

We present the models for the gas-phase, kinetic nucleation and bulk growth through condensation and surface reactions. In Sect. 2.1, we describe our chemical kinetics network of the gas-phase. The kinetic nucleation, which describes the time-dependent nucleation within disequilibrium environments, is described in Sect. 2.2 (two-body reactions) and in Sect. 2.3 (three-body reactions). In Sect. 2.4, we describe the bulk growth through condensation and surface reactions. The derivation of the reaction supersaturation is given in Sect. 2.5. Finally, the connection between nucleation and bulk growth is described in Sect. 2.6.

2.1. Gas-phase chemistry

The evolution of the number density n_i [cm^{-3}] of a given species i is determined by the following equation:

$$\frac{dn_i}{dt} = \sum_{r \in F_i} \left(v_{i,r} k_r \prod_{j \in E_r} n_j \right) - \sum_{r \in D_i} \left(v_{i,r} k_r \prod_{j \in E_r} n_j \right), \quad (1)$$

where F_i the set of reactions where the i -th species is a product, D_i the set of reactions where the i -th species is a reactant, E_r the set of reactants of reaction r , n_j [cm^{-3}] the number densities of the reactants, $v_{i,r}$ the stoichiometric coefficient of the i -th species within reaction r , k_r [$\text{cm}^{3(J_r-1)}\text{s}^{-1}$] the reaction rate for the reaction r and J_r the number of reactants in E_r . The sum over all n_j is the total number density. The numerical solver is described in Appendix A.

Chemical kinetic networks for the atmospheres of exoplanets include several hundred species and several thousand reactions (e.g. Rimmer & Helling 2016; Tsai et al. 2017, 2021; Venot et al. 2012, 2020). For this paper, we chose the "NCHO thermo network" of VULCAN^{1,2} (Tsai et al. 2017, 2021). This network includes 69 species and 780 reactions. In this work, TiO_2 is considered as the nucleation species. Because "NCHO thermo network" of VULCAN does not include reactions for the formation of TiO_2 , we add several reactions from Boulangier et al. (2019) leading to the formation of TiO_2 . The selected gas-phase reactions can be found in Table E.1. Furthermore, we add reactions including Si species for the bulk growth species SiO and SiO_2 (see Sect. 2.4 and Table E.1).

All calculations start from chemical equilibrium abundances calculated using GGchem (Woitke & Helling 2021) for a solar-like composition (Asplund et al. 2009). A list of the considered species for the equilibrium calculation is given in Appendix B.

2.2. Nucleation

Nucleation reaction networks are ideally constructed by considering multiple reaction pathways. Unfortunately, only few such studies exist (see e.g. Bromley et al. 2016; Gobrecht et al. 2022; Andersson et al. 2023). In the kinetic network approach, the change in cluster number densities can be described as:

$$\frac{dn_N}{dt} = \sum_{r \in F_N} \left(v_{N,r} k_r^+ \prod_{j \in E_r} n_j \right) - \sum_{r \in D_N} \left(v_{N,r} k_r^- \prod_{j \in E_r} n_j \right), \quad (2)$$

where n_N [cm^{-3}] is the number density of a given polymer of size N (also called N -mer), F_N is the set of forward reactions involving the N -mer, D_N is the set of backward reactions involving the N -mer. k_r^+ [$\text{cm}^{3(J_r-1)}\text{s}^{-1}$] is the forward reaction rate coefficient of reaction r , k_r^- [$\text{cm}^{3(J_r-1)}\text{s}^{-1}$] is the backward reaction rate coefficient of reaction r and J_r is the number of reactants.

We describe the growth reactions of nucleating species as two-body reactions ($a + b \rightarrow c$). The forward reaction rate coefficient k_r^+ can then be described as (Peters 2017; Boulangier et al. 2019):

$$k_r^+ = \int_0^\infty \alpha_r(v_r) \sigma_r(v_r) v_r f(v_r) dv_r, \quad (3)$$

¹ https://github.com/exoclimate/VULCAN/blob/master/thermo/NCHO_thermo_network.txt

² A comparison to the chemical kinetics networks of Decin et al. (2018) and Gobrecht et al. (2022) can be found in Appendix D.

where v_r [cm s⁻¹] is the relative velocity of the collision partners, $\alpha_r(v_r)$ the sticking coefficient, $\sigma_r(v_r)$ [cm²] is the reaction cross section and $f(v_r)$ the relative velocity distribution of the colliding particles. Similar to other work, we set the sticking coefficient $\alpha_j(v_r)$ to 1 because detailed values for nucleation reactions are not available so far (e.g. Lazzati 2008; Bromley et al. 2016; Boulanger et al. 2019). The cross section is approximated by a collision of two hard spheres:

$$\sigma_j = \pi(r_1 + r_2)^2, \quad (4)$$

where r_1 and r_2 [cm] are the interaction radii of the reaction partners. For this work, we consider radii including electrostatic forces (Köhn et al. 2021; Gobrecht et al. 2022; Kiefer et al. 2023). The relative velocity distribution is described by a Maxwell-Boltzmann distribution:

$$f(v_r) = \left(\frac{\mu}{2\pi k_B T_{\text{gas}}}\right)^{3/2} 4\pi v_r^2 \exp\left(-\frac{\mu v_r^2}{2k_B T}\right), \quad (5)$$

where T_{gas} [K] is the temperature, $k_B = 1.381 \times 10^{-23}$ erg K⁻¹ is the Boltzmann constant and

$$\mu = \frac{m_1 m_2}{(m_1 + m_2)} \quad (6)$$

is the reduced mass [g] with m_1 , m_2 [g] being the masses of the reaction partners. Solving the integral from Eq. 3 yields:

$$k_j^+ = \pi(r_1 + r_2)^2 \sqrt{\frac{8k_B T_{\text{gas}}}{\pi\mu}}. \quad (7)$$

The backwards reaction rate (c → a + b) is derived by assuming detailed balance. For this, an equilibrium state needs to be defined which we assume to be the chemical equilibrium state such that the law of mass action can be applied:

$$k_j^- = k_j^+ \frac{p^\ominus}{k_B T_{\text{gas}}} \exp\left(\frac{G_c^\ominus(T_{\text{gas}}) - G_a^\ominus(T_{\text{gas}}) - G_b^\ominus(T_{\text{gas}})}{k_B T_{\text{gas}}}\right), \quad (8)$$

where $p^\ominus = 10^5$ Pa is the standard pressure and $G_i^\ominus(T_{\text{gas}})$ [erg] is the Gibbs free energy of an i -mer at standard pressure.

For this study, we consider TiO₂ as nucleating species. The chemical network is extended by including all forward (Eq. 3) and backward reactions (Eq. 8) from the monomer up to the 15-mer. The Gibbs free energy data is taken from Sindel et al. (2022).

2.3. Three-body reactions for cluster formation

Three-body reactions are important for the formation of small clusters. On the one hand, third bodies can remove the energy of formation from an association (forward) reaction thus increasing cluster formation rates. On the other hand, collisions with third bodies can induce dissociation (backward) reactions. For this work, we consider three-body reactions for the cluster formation of TiO₂ up to (TiO₂)₄. The reaction rates are taken from Kiefer et al. (2023) (see reactions number RNr 19 to 26 in Table E.1).

To analyse for which temperature and pressures three-body reactions dominate over two-body reactions, we compare the reaction rate coefficients. To allow a direct comparison, we multiply the reaction rate coefficients with the number density of third bodies. The comparison can be seen in Fig. 1. For reaction RNr 19 and 20, multiple pressures are shown. Since all three-body

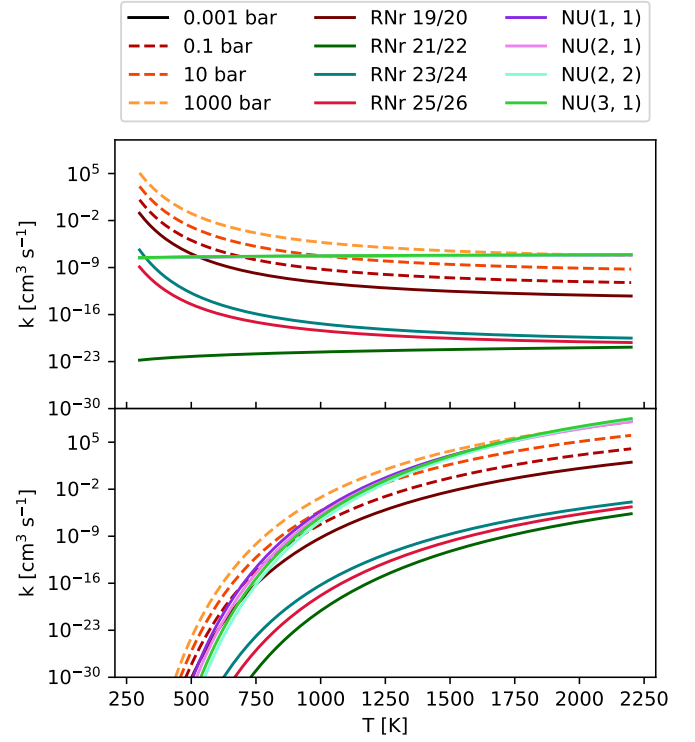


Fig. 1. Reaction rate coefficients for the formation of TiO₂ clusters up to (TiO₂)₄. All solid lines assume $p_{\text{gas}} = 0.002$ bar. **Top:** Association reactions. **Bottom:** Dissociation reactions.

reactions have the same pressure dependence, the scaling is the same for all of them. For two-body reactions, we use the following shorthand notation:



For the association and dissociation of (TiO₂)₂ from and into two monomers respectively (RNr 19/20 and NU(1, 1)), the three-body reaction becomes dominant below $T_{\text{gas}} = 400$ K and for pressures higher than $p_{\text{gas}} = 0.001$ bar. Above $T_{\text{gas}} = 1300$ K and for pressures lower than $p_{\text{gas}} = 10$ bar, the two-body reaction becomes dominant. In between, either type of reaction can be dominant. At higher pressures (e.g. $p_{\text{gas}} > 1000$ bar), the three-body reaction becomes dominant even at high temperatures (e.g. $T_{\text{gas}} > 2000$ K). For all other reactions compared in this section (RNr 21/22, 23/24, 25/26 and NU(2, 1), NU(2, 2), and NU(3, 1)), the two-body reaction typically dominates above $T_{\text{gas}} > 400$ K. Three-body reactions only start to become important at very high pressures (e.g. $p_{\text{gas}} > 1000$ bar).

2.4. Bulk growth

In order to describe the bulk growth by gas-surface reaction we apply the moment method (Gail & Sedlmayr 1986, 1988; Dominik et al. 1993; Helling et al. 2001; Helling & Woitke 2006). The j -th moment L_j [cm ^{j} g⁻¹] is defined as:

$$\rho L_j = \int_{V_l}^{\infty} f(V) V^{j/3} dV, \quad (10)$$

where $j \in \{0, 1, 2, 3\}$, V [cm³] is the cloud particle volume, V_l [cm³] is the minimum volume of a cloud particle to start bulk growth, ρ [cm⁻³] the gas density and $f(V)$ [cm⁻⁶] is the cloud

particle size distribution function. Using these moments the following cloud particle properties can be derived (Gail & Sedlmayr 1988; Helling et al. 2001):

$$n_d = \rho L_0, \quad (11)$$

$$\langle a \rangle = \sqrt[3]{\frac{3}{4\pi} \frac{\rho L_1}{\rho L_0}}, \quad (12)$$

$$\langle A \rangle = \sqrt[3]{36\pi} \frac{\rho L_2}{\rho L_0}, \quad (13)$$

$$\langle V \rangle = \frac{\rho L_3}{\rho L_0}, \quad (14)$$

where n_d [cm⁻³] is the cloud particle number density, $\langle a \rangle$ [cm] the mean cloud particle radius, $\langle A \rangle$ [cm²] the mean cloud particle surface area and $\langle V \rangle$ [cm³] the mean cloud particle volume. The change in the moments is determined by the nucleation and bulk growth and is described by the following set of equations³ (Helling & Woitke 2006):

$$\frac{\partial}{\partial t} \rho L_0 = J_\star(V_l), \quad (15)$$

$$\frac{\partial}{\partial t} \rho L_j = V_l^{j/3} J_\star(V_l) + \frac{j}{3} \chi^{\text{net}} \rho L_{j-1}, \quad (16)$$

$$\chi^{\text{net}} = \sqrt[3]{36\pi} \sum_{r \in C_d} \Delta V_r n_r^{\text{key}} \langle v_r \rangle \frac{\alpha_r(v_r)}{v_r^{\text{key}}} \left(1 - \frac{1}{(S_r)^{1/v_r^{\text{key}}}} \frac{1}{b_r^{\text{surf}}} \right), \quad (17)$$

where $J_\star(V_l)$ [cm⁻³] is the nucleation rate (see Sect. 2.6), C_d is the set of surface reactions, ΔV_r [cm³] is the volume increase per surface reaction r , n_r^{key} [cm⁻³] is the number density of the key gas-phase species, v_r^{key} is the stoichiometric coefficient of the key gas-phase species for the surface reaction r , $\langle v_r \rangle$ [cm s⁻¹] is the average relative velocity between the cloud particle and the key gas-phase species, S_r is the reaction supersaturation (see section 2.5) and b_r^{surf} the surface area fraction of the given bulk growth material. χ^{net} [cm s⁻¹] is the net growth velocity. The key gas-phase species is the least abundant species involved in a given bulk growth reaction (Woitke & Helling 2003; Helling & Woitke 2006). The left term in the bracket of Eq. 17 represents the growth and the right term represents the evaporation. The cloud particle grows if the net sign of the bracket is positive and evaporates if the sign is negative. Similar to Helling & Woitke (2006), we assume that the surface area fraction can be approximated by the volume fraction:

$$b_r^{\text{surf}} = \frac{A_r}{A_{\text{tot}}} \approx \frac{V_r}{V_{\text{tot}}}, \quad (18)$$

where A_{tot} [cm²] is the total cloud particle surface area and V_{tot} [cm³] is the total cloud particle volume. The volume fraction of each cloud particle material is tracked separately.

The growth of cloud particles through bulk growth depletes the gas-phase. Therefore, we adjust the number densities n_i of the species i involved in the surface reaction r (Helling & Woitke 2006):

$$\frac{dn_i}{dt} = \delta(i) v_{i,r} \chi^{\text{net}} \frac{\rho L_2}{\Delta V_r}, \quad (19)$$

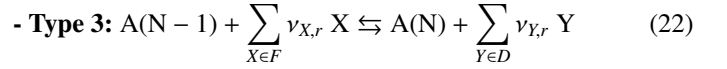
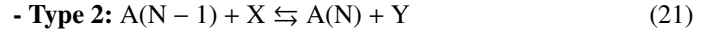
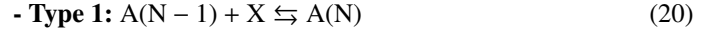
where $\delta(i)$ is equal to 1 for products and -1 for reactants.

³ Gravitational settling and other transport processes may be added as source terms to the r.h.s., (Woitke & Helling 2003)

For this study, we consider TiO₂[s], Al₂O₃[s], SiO[s], SiO₂[s], MgO[s], Mg₂SiO₄[s], FeO[s], FeS[s], Fe₂O₃[s] and Fe₂SiO₄[s] as bulk growth materials and include the surface reactions listed in Table E.2.

2.5. Reaction Supersaturation

To calculate the net growth velocity as described in Eq. 17, the reaction supersaturation needs to be calculated. Surface growth and evaporation of a material s can occur via three types of reactions:



where X is a reactant, Y a product, A(N) a cloud particle containing N units of bulk growth material⁴ (e.g. Mg₂SiO₄ would be 1 unit for Mg₂SiO₄[s]), F the set of reactants, D the set of products and $\nu_{i,r}$ the stoichiometric coefficients of species i for the surface reaction r . Type 1 reactions describe condensation, Type 2 reactions are chemical growth reactions, and Type 3 reactions involve surface chemistry. Cloud particles are assumed to be large enough for the following approximation to hold:

$$G_{A(N)}^\ominus \approx G_{A(N-1)}^\ominus + G_A^\ominus, \quad (23)$$

where $G_{A(N)}^\ominus$ [erg] is the Gibbs free energy of formation at standard pressure of the A(N) cloud particle made from N units and G_A^\ominus [erg] is the Gibbs free energy of formation of a solid unit at standard pressure. The goal of this section is to find the reaction supersaturation S_r of these reactions defined as:

$$S_r = \frac{R_f}{R_b}, \quad (24)$$

where R_f [s⁻¹] is the growth rate and R_b [s⁻¹] is the evaporation rate. It is important to note that the following derivations are done in chemical disequilibrium. At no point in this section do we assume chemical equilibrium.

2.5.1. S_r of Type 1 reactions (condensation)

Type 1 reactions are reactions where the reactant is also the bulk growth material. In this case the reaction supersaturation is equal to the supersaturation of the growth species:

$$S_r = S = \frac{p_X}{p_X^{\text{vap}}} = \frac{n_X}{k_B T} \frac{1}{p^\ominus} \exp\left(\frac{G_X^\ominus - G_A^\ominus}{k_B T_{\text{gas}}}\right), \quad (25)$$

where p_X^{vap} [dyn cm⁻²] is the vapour pressure of species X, p_X [dyn cm⁻²] is the partial pressure of species X, n_X [cm⁻³] the gas-phase number density of species X, T_{gas} [K] the temperature, and G_X^\ominus [erg] the Gibbs free energy of formation of the condensing species in the gas-phase at standard pressure. Since the bulk growth material exists in the gas-phase, the supersaturation is well defined.

⁴ A(N) can be heterogeneous and contain multiple bulk growth materials. To simplify notation, we only note the number of bulk growth units N of the bulk growth material involved in a given reaction.

2.5.2. S_r of Type 2 reactions

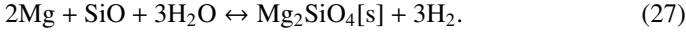
Type 2 reactions were discussed in detail in previous studies (Gail & Sedlmayr 1988; Gauger et al. 1990; Dominik et al. 1993; Patzer et al. 1998). The reaction supersaturation is given by (adapted from Patzer et al. 1998):

$$S_r = \frac{n_X}{n_Y} \exp\left(\frac{G_X^\ominus - G_Y^\ominus - G_A^\ominus}{k_B T_{\text{gas}}}\right), \quad (26)$$

where G_X^\ominus [erg] and G_Y^\ominus [erg] are the Gibbs free energies of formation of the gas-phase reactant and product, respectively. n_X [cm^{-3}] is the number density of the reactant X and n_Y [cm^{-3}] is the number density of the product Y. Type 2 reactions are well defined even if the bulk growth material is not present in the gas-phase (see Patzer et al. (1998) for further details).

2.5.3. S_r of Type 3 reactions

Type 3 reactions involve surface chemistry. Considering these reactions is especially important if the bulk growth material is not present in the gas-phase. For example, $\text{Mg}_2\text{SiO}_4[\text{s}]$ can condense via the surface reaction



To simplify the notation, we use the reaction of Eq. 27 as an example for this section and generalise the results in the end. For our example in this section, we assume Mg to be the key gas-phase species. The bulk growth rate of this reaction can then be described by (adapted from Helling & Woitke 2006):

$$R_f = \left[A_{A(N-1)} v_{\text{key}} \frac{1}{v_r} \right] n_{\text{key}}, \quad (28)$$

where $A_{A(N-1)}$ [cm^2] is the surface area of the $A(N-1)$ cloud particle, $n_{A(N-1)}$ [cm^{-3}] the number density of the $A(N-1)$ cloud particle, v_{key} [cm s^{-1}] the relative velocity of the cloud particle and the key gas-phase species (e.g. Mg), and n_{key} [cm^{-3}] the number density of the key gas-phase species (e.g. Mg). Phase equilibrium for a given bulk growth reaction (short PGR, noted with $^\circ$) is characterised⁵ by the evaporation rate equalling the growth rate ($R_f^\circ = R_b^\circ$). Therefore according to Eq. 28, the evaporation rate is:

$$R_b = \left[A_{A(N-1)} v_{\text{key}} \frac{1}{v_r} \right] n_{\text{key}}^\circ, \quad (29)$$

where n_{key}° [cm^{-3}] is the number density of the key gas-phase species in PGR (e.g. Mg). Since all non-key gas-phase species are typically much more abundant than the key gas-phase species, their number densities in non-PGR only slightly differ to their number densities in PGR. Therefore, the following approximation holds:

$$\frac{n_{\text{SiO}}^\circ}{n_{\text{SiO}}} \approx \frac{n_{\text{H}_2\text{O}}^\circ}{n_{\text{H}_2\text{O}}} \approx \frac{n_{\text{H}_2}^\circ}{n_{\text{H}_2}} \approx 1. \quad (30)$$

⁵ In this section until and with Eq. 41, PGR is towards the reaction from Eq. 27 but the same derivation holds for an arbitrary reaction of type 3.

This allows us to write the reaction supersaturation as:

$$\begin{aligned} S_r^2 &= \frac{(n_{\text{Mg}})^\circ}{(n_{\text{Mg}})^\circ} = \frac{(n_{\text{Mg}})^\circ n_{\text{SiO}}^\circ (n_{\text{H}_2\text{O}}^\circ)^3 (n_{\text{H}_2}^\circ)^3}{(n_{\text{Mg}})^\circ n_{\text{SiO}}^\circ (n_{\text{H}_2\text{O}}^\circ)^3 (n_{\text{H}_2}^\circ)^3} \left[\frac{n_{\text{SiO}} (n_{\text{H}_2\text{O}})^3 (n_{\text{H}_2}^\circ)^3}{n_{\text{SiO}}^\circ (n_{\text{H}_2\text{O}}^\circ)^3 (n_{\text{H}_2}^\circ)^3} \right] \\ &\approx \frac{(n_{\text{Mg}})^\circ n_{\text{SiO}} (n_{\text{H}_2\text{O}})^3}{(n_{\text{H}_2}^\circ)^3} \frac{(n_{\text{H}_2}^\circ)^3}{(n_{\text{Mg}})^\circ n_{\text{SiO}}^\circ (n_{\text{H}_2\text{O}}^\circ)^3}, \end{aligned} \quad (31)$$

leaving only the ratios of gas number densities in PGR to find.

We start the derivation with a thought experiment. Imagine a box containing a given elemental abundance of Mg, SiO, H_2O , H_2 , $A(N-1)$ and $A(N)$. We assume that in this box, gas-phase species only react with each other via the specific surface reaction from Eq. 27 but do not react with each other otherwise. Over time, the box will evolve towards PGR for this specific chemical configuration. In PGR, the entropy of the box will be maximised which is equivalent to minimising the Gibbs free energy for the reactants and products of the given reaction. This minimisation problem with its constraints can be expressed in the following Lagrangian function:

$$\begin{aligned} \mathcal{L} &= \left[\sum_{j \in E} N_j G_j^\ominus + N_j k_B T_{\text{gas}} \ln \left(\frac{N_j}{N} \right) \right] \\ &+ \lambda_1 (C_1 + N_{\text{Mg}} - 2N_{\text{SiO}}) \\ &+ \lambda_2 (C_2 + 3N_{\text{Mg}} - 2N_{\text{H}_2\text{O}}) \\ &+ \lambda_3 (C_3 + N_{\text{Mg}} - 2N_{A(N-1)}) \\ &+ \lambda_4 (C_4 - 3N_{\text{Mg}} - 2N_{\text{H}_2}) \\ &+ \lambda_5 (C_5 - N_{\text{Mg}} - 2N_{A(N)}), \end{aligned} \quad (33)$$

where $E = \{\text{Mg}, \text{SiO}, \text{H}_2\text{O}, \text{H}_2, A(N-1), A(N)\}$ is the set of particles, N_j the total number of particles j , N is the total number of gas particles, G_j^\ominus [erg] the Gibbs free energy of formation of particle j at standard pressure, λ_i [erg] are the Lagrangian multipliers and C_i are constants. The constraints from λ_1 , λ_2 , and λ_3 are keeping the ratio of Mg, SiO, H_2O and $A(N-1)$ per reaction constant using Mg as reference. The constraints from λ_4 , and λ_5 ensure mass conservation. Minimizing this Lagrangian for all molecules and cloud particles results in the following set of equations:

$$\frac{d\mathcal{L}}{dN_{\text{Mg}}} = G_{\text{Mg}}^\ominus + k_B T_{\text{gas}} \ln \left(\frac{N_{\text{Mg}}}{N} \right) + \lambda_1 + 3\lambda_2 + \lambda_3 - 3\lambda_4 - \lambda_5, \quad (34)$$

$$\frac{d\mathcal{L}}{dN_{\text{SiO}}} = G_{\text{SiO}}^\ominus + k_B T_{\text{gas}} \ln \left(\frac{N_{\text{SiO}}}{N} \right) - 2\lambda_1, \quad (35)$$

$$\frac{d\mathcal{L}}{dN_{\text{H}_2\text{O}}} = G_{\text{H}_2\text{O}}^\ominus + k_B T_{\text{gas}} \ln \left(\frac{N_{\text{H}_2\text{O}}}{N} \right) - 2\lambda_2, \quad (36)$$

$$\frac{d\mathcal{L}}{dN_{A(N-1)}} = G_{A(N-1)}^\ominus + k_B T_{\text{gas}} \ln \left(\frac{N_{A(N-1)}}{N} \right) - 2\lambda_3, \quad (37)$$

$$\frac{d\mathcal{L}}{dN_{\text{H}_2}} = G_{\text{H}_2}^\ominus + k_B T_{\text{gas}} \ln \left(\frac{N_{\text{H}_2}}{N} \right) - 2\lambda_4, \quad (38)$$

$$\frac{d\mathcal{L}}{dN_{A(N)}} = G_{A(N)}^\ominus + k_B T_{\text{gas}} \ln \left(\frac{N_{A(N)}}{N} \right) - 2\lambda_5. \quad (39)$$

In PGR, the Lagrangian function is minimal and thus the derivatives are zero. Solving this set of equations, using the approximation of Eq. 23, and going from particle numbers N_j to particle

number densities n_j leads to:

$$\frac{(n_{\text{Mg}}^\circ)^2 n_{\text{SiO}}^\circ (n_{\text{H}_2\text{O}}^\circ)^3}{(n_{\text{H}_2}^\circ)^3} \approx \left(\frac{p^\ominus}{k_B T_{\text{gas}}} \right)^3 \exp \left(\frac{-1}{k_B T_{\text{gas}}} \left[2G_{\text{Mg}}^\ominus + G_{\text{SiO}}^\ominus + 3G_{\text{H}_2\text{O}}^\ominus - 3G_{\text{H}_2}^\ominus - G_{\text{Mg}_2\text{SiO}_4[\text{S}]}^\ominus \right] \right). \quad (40)$$

This result gives us the relation between the number densities of the reactants and products of the bulk growth reaction. Hence, the reaction supersaturation for the reaction of Eq. 27 is given by:

$$S_r^{\text{vkey}} \approx \frac{(n_{\text{Mg}}^\circ)^2 n_{\text{SiO}}^\circ (n_{\text{H}_2\text{O}}^\circ)^3}{(n_{\text{H}_2}^\circ)^3} \left(\frac{p^\ominus}{k_B T_{\text{gas}}} \right)^{-3} \exp \left(\frac{1}{k_B T_{\text{gas}}} \left[2G_{\text{Mg}}^\ominus + G_{\text{SiO}}^\ominus + 3G_{\text{H}_2\text{O}}^\ominus - 3G_{\text{H}_2}^\ominus - G_{\text{Mg}_2\text{SiO}_4[\text{S}]}^\ominus \right] \right). \quad (41)$$

For an arbitrary type 3 reaction that is limited by a key gas-phase species, the reaction supersaturation is then given by:

$$S_r^{\text{vkey}} = \frac{\prod_{X \in F} n_X^{\nu_X}}{\prod_{Y \in D} n_Y^{\nu_Y}} \left(\frac{p^\ominus}{k_B T_{\text{gas}}} \right)^{l_Y - l_X} \exp \left(\frac{1}{k_B T_{\text{gas}}} \left[G_A^\ominus - \sum_{X \in F} \nu_X G_X^\ominus + \sum_{Y \in D} \nu_Y G_Y^\ominus \right] \right), \quad (42)$$

where l_X is the number of reactants and l_Y is the number of products. If only 1 reactant is considered, this result matches the result for type 1 reactions. It also matches type 2 reactions if only 1 key reactant and 1 key product are considered. In the case of chemical equilibrium, our description of the supersaturation ratio for type 3 reactions is the same as the one found by [Helling & Woitke \(2006\)](#).

We define the right hand side of Eq. 40 as the reaction vapor coefficient c_r^{vap} [$\text{cm}^{-3(l_X - l_Y)}$] and fit it with:

$$\ln \left(\frac{c_r^{\text{vap}}}{[\text{cm}^{-3(l_X - l_Y)}]} \right) = \sum_{i=0}^3 \frac{s_i}{T_{\text{gas}}^i}. \quad (43)$$

The fitting parameters for the surface reactions considered in this paper are given in Table E.2. This allows us to write the reaction supersaturation as:

$$S_r^{\text{vkey}} = \frac{\prod_{X \in F} n_X^{\nu_X}}{\prod_{Y \in D} n_Y^{\nu_Y}} \frac{1}{c_r^{\text{vap}}}. \quad (44)$$

2.6. Formation rate of CCNs

To describe nucleation kinetically, we require the properties of each considered cluster size up until the size N_\star where the clusters become preferably thermally stable. For this, the Gibbs free energies G_N (Eq. 8), the interaction radii r_N (Eq. 4 and 7) and the masses m_N (Eq. 6) of all considered cluster sizes need to be known. Unfortunately, only limited data is available (see for example the case of TiO_2 : [Qu & Kroes 2006](#); [Lundqvist et al. 2006](#); [Zhai & Wang 2007](#); [Chiodo et al. 2011](#); [Lee et al. 2015](#); [Sindel et al. 2022](#)). We use the data of [Sindel et al. \(2022\)](#) and approximate the nucleation rate with the largest cluster for which all necessary data is available, which in this case is $N_{\text{max}} = 15$. The quality of this assumption for N_{max} is tested in Sect. 3.3.

We follow the approach of [Patzer et al. \(1998\)](#) and calculate the nucleation rate as:

$$J_\star(V_l) = \frac{dn_{N_{\text{max}}}}{dt}, \quad (45)$$

which describes the rate at which CCNs are formed. The growth from clusters made from N_{max} monomers to clusters with a volume of V_l depletes the gas-phase of the clustering species. Because polymer nucleation is considered, all N-mers up to a given Q -mer are depleted:

$$\frac{dn_N}{dt} = -J_\star(V_l) \frac{n_N}{\omega_m}, \quad (46)$$

$$\omega_m = \frac{V_l}{\Delta V_r} \sum_{N=1}^Q N n_N, \quad (47)$$

where n_N [cm^{-3}] are N-mer number densities and $1 \leq N \leq Q$. For TiO_2 , the change in the number density of clusters of size $N_{\text{max}} = 15$ defines nucleation (see Eq. 45). We therefore exclude this size in the depletion description and select $Q_{\text{TiO}_2} = 14$.

Starting from V_l , the particles can grow via surface growth. Similarly, they can shrink via evaporation down to size V_l . To numerically separate between evaporation and nucleation, cloud particles should only evaporate down to size V_l . For the ODE solver, we need a continuous transition and therefore adjust the evaporating surface area by multiplying the evaporation term of Eq. 17 with

$$c_{\text{vol}} = \left(\frac{\rho L_3}{\rho L_0} - V_l \right) \frac{\rho L_0}{\rho L_3}. \quad (48)$$

Including Eq. 48 in Eq. 17 results in:

$$\chi^{\text{net}} = \sqrt[3]{36\pi} \sum_{r \in C_d} \Delta V_r n_r^{\text{key}} \langle v_r \rangle \frac{\alpha_r(v_r)}{v_r^{\text{key}}} \left(1 - \frac{c_{\text{vol}}}{S_r^{1/\nu_r^{\text{key}}} b_r^{\text{surf}}} \right). \quad (49)$$

For the rest of this paper, we are using Eq. 49 for χ^{net} in Eqs. 16 and 19.

3. Exploring kinetic chemistry and nucleation

In Sect. 3.1, we create a chemical network for the kinetic cloud formation model. Using this network, we study the impact on the gas phase when combining different chemical kinetics networks, nucleation and bulk growth. Describing bulk growth fully time dependent revealed a SiO-SiO_2 cycle within the surface reactions which is discussed in Sect. 3.2. In Sect. 3.3, we evaluate the nucleation rate's dependence on different maximum cluster sizes N_{max} .

3.1. A chemical network for kinetic cloud formation

To find the impact of combining different chemical networks, nucleation and bulk growth on the number densities of the gas-phase species, we compare the gas-phase abundances in 4 cases:

- **Equilibrium:** Chemical equilibrium number densities calculated using GGchem. This calculation is time independent.
- **VULCAN:** The "NCHO thermo network" reactions of VULCAN.

- **VULCAN+**: This network combines the "NCHO thermo network" reactions of VULCAN, and the Ti and Si reactions as listed in Table E.1
- **VULCAN+poly**: This network combines the "NCHO thermo network" reactions of VULCAN, the Ti and Si reactions as listed in Table E.1, the polymer nucleation reactions for TiO_2 as described in Sect. 2.2, and the formation of TiO_2 CCNs as described in Sect. 2.6.
- **Full**: This network combines the "NCHO thermo network" reactions of VULCAN, the Ti and Si reactions as listed in Table E.1, the polymer nucleation reactions for TiO_2 as described in Sect. 2.2, the formation of TiO_2 CCNs as described in Sect. 2.6, and the bulk growth through condensation and surface reactions as described in Sect. 2.4.

All simulations start from equilibrium number densities calculated with GGchem. All time axis in this paper measure the evaluation time t [s] of the disequilibrium chemistry starting from equilibrium conditions at $t = 0$ s. The results for the $T_{\text{gas}}-p_{\text{gas}}$ point⁶ $p_{\text{gas}} = 0.002$ bar at $T_{\text{gas}} = 1378$ K can be seen in Fig. 2. The chemical equilibrium number densities match the predicted number densities of VULCAN and are therefore not shown in the figure.

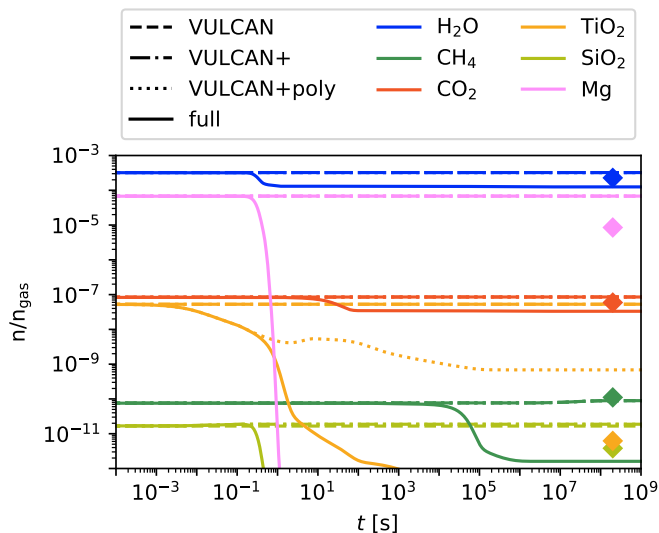


Fig. 2. Concentrations of selected gas-phase species for $p_{\text{gas}} = 0.002$ bar at $T_{\text{gas}} = 1378$ K using different chemical kinetics networks. The diamond shaped marker show GGchem results including equilibrium condensation.

To compare the difference in the predicted number densities, we compare the maximum absolute difference between the logarithm of the number densities of species A between two chemical networks C_1 and C_2 :

$$P(A, C_1, C_2) = \max\{|\log_{10}(n_{C_1}^A(t)/n_{C_2}^A(t))|, \forall t \in [10^{-4}, 10^9]\}. \quad (50)$$

The P values for $p_{\text{gas}} = 0.002$ bar and $T_{\text{gas}} = 1378$ K, which represents a low-pressure level in a relatively cool atmosphere, are shown in Table 1. For the comparison we chose H_2 because it is the dominant gas phase species, H_2O and CO_2 because they are

⁶ This $T_{\text{gas}}-p_{\text{gas}}$ point corresponds to a location within the evening terminator of HD 209458 b.

commonly studied, methane (CH_4) because it has distinct spectral features, Mg and SiO_2 because they are condensing species, and TiO_2 because it is the nucleating species.

Comparing Equilibrium to VULCAN and VULCAN to VULCAN+ shows in both cases close to no difference ($P < 0.1$) in the predicted number densities of H_2 , H_2O , CO_2 , CH_4 , and SiO_2 . In VULCAN+poly TiO_2 nucleation reactions and the formation of TiO_2 CCNs are added. Therefore, it comes at no surprise that the number density of TiO_2 decreases by close to two orders of magnitude. The impact for H_2 , H_2O , CO_2 , CH_4 , and SiO_2 on the other hand is still negligible. When bulk growth is added in the full network, the number densities of TiO_2 , SiO_2 and Mg decrease by several orders of magnitude due to being depleted by the bulk growth processes. The impact of bulk growth can also be seen in the number densities of H_2O , CO_2 , and CH_4 . The change in CH_4 is discussed in Sect. 3.2. The number density of H_2 on the other hand is not significantly affected.

Also shown in Fig. 2 are the gas-phase concentrations calculated using GGchem including the equilibrium condensation of the bulk grow materials. Compared to our results, GGchem equilibrium condensation results predict higher gas-phase concentrations in the cloud forming species TiO_2 , SiO_2 , and Mg as well as the gas-phase only species H_2O , CH_4 , and CO_2 . Because our work treats cloud formation kinetically, these differences can be caused by the nucleation or surface reactions which are both not considered within GGchem. In environments like the ISM or Titan's atmosphere, surface reactions are known to cause deviations from equilibrium gas-phase abundances (see Sect. 3.2).

Selecting a suitable gas-phase chemical kinetics network is important. We chose VULCAN because it includes commonly considered species such as H_2O , CO_2 and CH_4 with a reasonably low number of reactions (780). Other chemical kinetics networks for exoplanet atmospheres include thousands of reactions (e.g. Venot et al. 2012; Venot & Agúndez 2015; Rimmer & Helling 2016; Hobbs et al. 2019; Venot et al. 2020). Because of the computational intensity of these networks, their evaluation is often limited to 1D models (e.g. Moses et al. 2005; Chadney et al. 2017; Hobbs et al. 2022; Barth et al. 2021). Adding kinetic nucleation and bulk growth to the chemical network can increase the computational time considerably. For the simulations in this section, the evaluation time doubled if nucleation and bulk growth were considered. If enough computational resources are available, our kinetic nucleation and bulk growth model can be combined with extensive chemical networks for a detailed study. Furthermore, models and observations have shown that the 3D structure of exoplanets can have an impact on the gas-phase chemistry (Baeyens et al. 2021; Prinoth et al. 2022; Lee et al. 2023). To evaluate the chemistry and cloud formation within 3D models, the cloud formation description can be combined with small but accurate networks (Tsai et al. 2022).

Most chemical kinetics networks for exoplanet atmospheres do not include many Mg, Ti, Si, or Fe bearing species. In our simulations, only the surface reactions c0, c1, c2, c4, c16, c71, c80, c85, c101, and c104 (see Table E.2) have all reactants and products within the chemical kinetics network. All other bulk growth reactions rely at least partially on gas-phase species which are only calculated in equilibrium. Ideally, all reactants and products of surface reactions should be included in the chemical kinetics network but they are not always available in literature and would drastically increase the number of reactions.

Table 1. Offset values between the number densities of given molecular species for different chemical networks according to Eq. 50.

	H ₂	H ₂ O	CO ₂	CH ₄	TiO ₂	SiO ₂	Mg
$P(A, \text{Equilibrium, VULCAN})$	4.84e-05	7.35e-03	1.58e-02	6.35e-02	-	-	-
$P(A, \text{VULCAN, VULCAN+})$	5.18e-11	1.34e-07	1.83e-05	1.18e-07	7.43e-04	5.25e-02	-
$P(A, \text{VULCAN+}, \text{VULCAN+poly})$	4.99e-08	1.32e-04	1.49e-04	1.32e-04	1.89	1.32e-04	-
$P(A, \text{VULCAN+poly, full})$	1.49e-03	0.41	0.41	1.74	5.21	2.35	12.8

3.2. SiO-SiO₂ cycle

In a fully kinetic description of cloud formation, minor species are affected as well. As shown in Fig. 2, adding bulk growth reactions significantly impacts the number density of CH₄, even though it is not directly involved in any bulk growth processes. This is important since CH₄ is discussed as bio molecule in terrestrial atmospheres (Thompson et al. 2022; Huang et al. 2022) and is observable in hot Jupiter atmospheres (Swain et al. 2009; Barman et al. 2015; Guilluy et al. 2019).

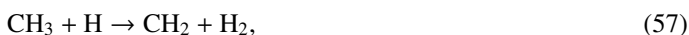
The 4 bulk growth reaction causing the decrease in CH₄ are c17, c19, c42, and c44. A closer look at these surface reactions revealed the following cycle:



The net process of this cycle is:



This additional pathway for the dissociation of H₂ to H decreases the number density of CH₄ through the following reactions:



Most of the carbon from CH₄ is transferred into H₂CO with the following reaction:



The change in carbon chemistry then also impacts other species like HCN, HCO, and C₂H₂.

To investigate at which pressures and temperatures the SiO-SiO₂ cycle significantly impacts the CH₄ abundance, $P(\text{CH}_4, \text{Equilibrium, VULCAN+poly})$ values for a range of pressures and temperatures were calculated. The results are shown in Fig. 3. The difference in the CH₄ abundance is largest for pressures lower than $p_{\text{gas}} < 10^{-3}$ bar and for temperatures around 1300 K.

The surface reactions used in this work were derived using a stoichiometric argument (Helling & Woitke 2006; Helling et al. 2008, 2017, 2019). Unfortunately, more detailed studies of surface reactions of bulk growth materials are missing in literature. To determine if all surface reactions of the SiO-SiO₂ cycle are likely to occur in exoplanet atmospheres, further investigations are needed. Because other processes, like quenching or photochemistry, can have similar effects (Moses et al. 2011), it will be difficult to gain insights into surface reactions through observations.

Molaverdikhani et al. (2020) analysed the impact of clouds on the methane abundance. They found that clouds can increase

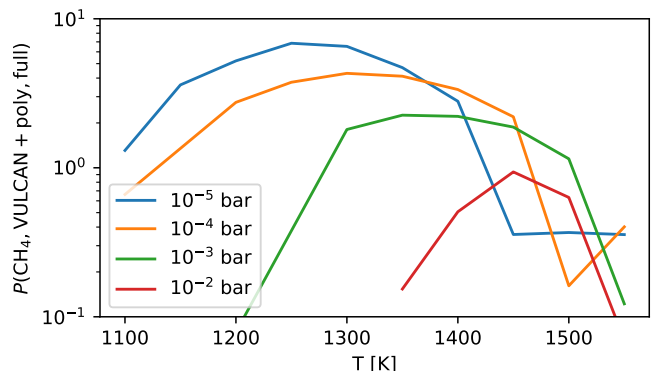


Fig. 3. Differences in the CH₄ abundance between chemical equilibrium and the VULCAN+poly network for various temperatures and pressures.

the temperature in the photo-sphere which in turn reduces the methane abundance. In contrast to our work, they used condensation curves rather than surface reactions and therefore they did not observe a direct impact of cloud formation on the CH₄ abundance.

In the (ISM) surface reaction are discussed as sources for molecular hydrogen in the gas phase (Hollenbach & Salpeter 1971; Williams 2005; Sabri et al. 2013; Dishoeck 2014; Herbst 2014, 2017). Similar to our study, in the ISM the surface of dust grains act as a catalyst but in contrast to our work, they do not result in bulk material being deposited. The calculation of ISM surface reaction rates typically accounts for the vibrational frequency of the reactants and the energy barriers between different sites on the dust particle (Dishoeck 2014). Our surface reaction description could be improved by similar considerations. However, the large number of surface reactions considered and the heterogeneity of the cloud particle make such evaluations difficult.

Similar to the ISM, the surfaces of aerosols in Titan's atmosphere can enhance the recombination of H into H₂ (Courtin et al. 1991; Bakes et al. 2003; Sekine et al. 2008). In addition, gas-phase catalytic cycles using hydrocarbons for the hydrogen recombination are postulated (Yung et al. 1984; Toublanc et al. 1995; Lebonnois et al. 2003). Both effects change the atomic hydrogen abundance which, similar to our work, can affect the abundance of hydrocarbons in return. In contrast to our work, the catalytic cycles considered are gas-phase only and do not result in bulk material being deposited.

3.3. Kinetic nucleation of TiO₂

To accurately model the CCN formation in exoplanet atmosphere, the nucleation rates of the dominant nucleating species need to be known. Previous studies determined TiO₂ (Goumans & Bromley 2013; Lee et al. 2015; Boulanger et al. 2019; Köhn et al. 2021) as an important nucleating species. Other species

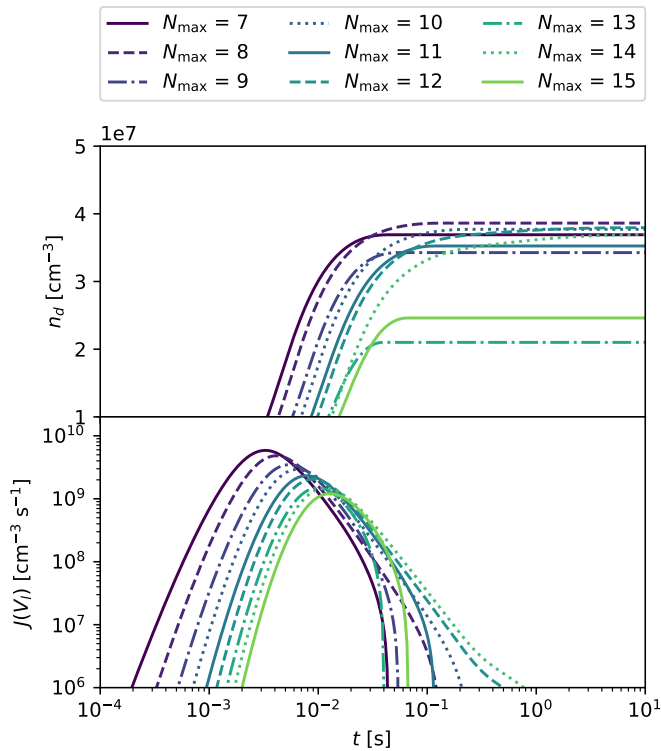


Fig. 4. Cloud particle number densities (**Top**) and nucleation rates (**Bottom**) for TiO_2 nucleation with different N_{\max} at $p_{\text{gas}} = 0.02$ bar and $T_{\text{gas}} = 1379$ K.

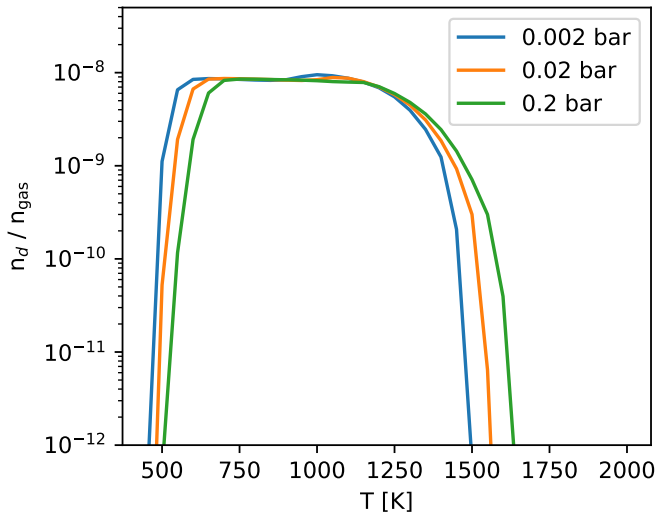


Fig. 5. Cloud particle concentrations for TiO_2 nucleation for a range of temperatures and pressures.

which are discussed as nucleating species are Al_2O_3 (Gobrecht et al. 2022), SiO (Gail & Sedlmayr 1986; Lee et al. 2015) and VO (Lecoq-Molinos et al. in prep). In addition to TiO_2 , we also analysed Al_2O_3 as a possible nucleating species for clusters up to size $N = 10$ (Gobrecht et al. 2022). The results were inconclusive (see Appendix C) and therefore, for this study, we decided to focus on TiO_2 .

If the maximum cluster size is larger than the smallest thermally stable cluster ($N_{\max} > N_\star$), the nucleation rate $J_\star(V_i)$ is expected to be independent of the choice of the maximum clus-

ter size. If the maximum cluster size is smaller than N_\star , we expect to see different nucleation rates depending on the choice of N_{\max} . Therefore, we test different N_{\max} ($7 \leq N_{\max} \leq 15$) and their impact on the cloud particle number density and nucleation rate. For this section, we set $p_{\text{gas}} = 0.02$ bar and $T_{\text{gas}} = 1379$ K. We use the full network as described in Sect. 3.1. The cloud particle number densities and nucleation rates for different N_{\max} can be seen in Fig. 4. The predicted number densities for $7 \leq N_{\max} \leq 15$ are all within a factor of 2. Furthermore, the peak in nucleation rate becomes smaller and appears later in time for larger clusters.

The biggest deviation in predicted cloud particle number density can be seen for $N_{\max} = 13$ and $N_{\max} = 15$ which predict lower cloud particle number densities than the rest. Looking at the Gibbs free energy per monomer unit ($G_{\text{TiO}_2(N)}^\ominus/N$) reveals that these sizes are the only N -mers that have a higher Gibbs free energy per monomer than their $(N-1)$ -mers:

$$\frac{G_{\text{TiO}_2(13)}^\ominus}{13} - \frac{G_{\text{TiO}_2(12)}^\ominus}{12} = 1.158, \quad (60)$$

$$\frac{G_{\text{TiO}_2(15)}^\ominus}{15} - \frac{G_{\text{TiO}_2(14)}^\ominus}{14} = 0.172. \quad (61)$$

Therefore, $N = 13$ and $N = 15$ are less thermally stable than their predecessors. Previous studies have shown the same preference for even N clusters (Lasserus et al. 2019) that we find for the $(\text{TiO}_2)_N$ clusters but further studies of larger sizes clusters are needed to determine if it is a size dependent trend that can affect the nucleation process. Because our nucleation rate is determined by the largest cluster size, having $N_{\max} = 13$ or $N_{\max} = 15$ naturally results in lower cloud particle number densities. Thermodynamic data for TiO_2 clusters larger than $N = 15$ is needed to further test this, and to find the thermally stable cluster size N_\star for TiO_2 .

Few studies have already evaluated nucleation using a non-classical approach. Lee et al. (2015) compared the nucleation rate predicted by CNT, MCNT and non-classical nucleation for various temperatures without considering surface growth. We calculated the cloud particle number density over the same temperature range as they analysed (Fig. 5). In contrast to our work, they considered only $N_{\max} = 10$ and only monomer nucleation. Both their and our study predict significant nucleation of TiO_2 for temperatures up to roughly 1300 K. Above that, the nucleation of TiO_2 quickly decreases. For temperatures between roughly 600 K to 1200 K, our model predicts approximately constant cloud particle number densities whereas the nucleation rate of Lee et al. (2015) decreases. This difference can be traced back to the polymer nucleation. Boulangier et al. (2019) showed that for TiO_2 and other nucleation seeds monomer nucleation can underestimate the formation of larger clusters in colder environments.

4. Time evolution of cloud formation in HD 209458 b

We simulate the chemistry and cloud formation for various $T_{\text{gas}}-p_{\text{gas}}$ points within HD 209458 b. The $T_{\text{gas}}-p_{\text{gas}}$ profiles used in this paper were calculated using expert/MITgcm simulations of HD 209458 b conducted by Schneider et al. (2022). The $T_{\text{gas}}-p_{\text{gas}}$ profiles for the sub-stellar point, anti-stellar point, evening terminator, and morning terminator can be seen in Fig. 6. The cloud particle concentrations and the mean cloud particle size as well as selected gas-phase concentrations and volume fractions⁷ for the sub-stellar point, evening terminator, anti-stellar

⁷ All volume fractions can be found in Fig. F.1.

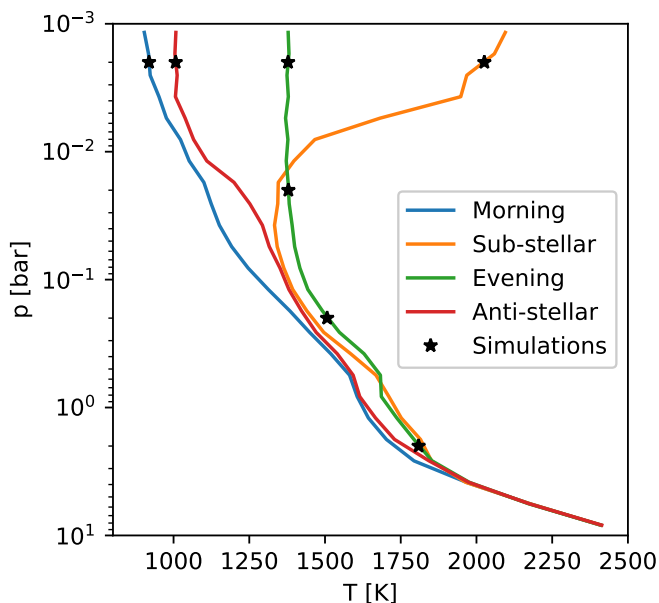


Fig. 6. $T_{\text{gas}}-p_{\text{gas}}$ profiles of HD 209458 b taken from Schneider et al. (2022). The $T_{\text{gas}}-p_{\text{gas}}$ points chosen for our simulations are marked with \star .

point and morning terminator at $p_{\text{gas}} = 0.002$ bar can be seen in Fig. 7. This pressure layer was selected as it showed the largest spread in temperatures. The results for 4 logarithmically spaced pressure points ($p_{\text{gas}} \in \{0.002 \text{ bar}, 0.02 \text{ bar}, 0.2 \text{ bar}, 2 \text{ bar}\}$) along the evening terminator can be seen in Fig. 8. Only one $T_{\text{gas}}-p_{\text{gas}}$ profile was selected since the temperatures deeper in the atmosphere ($p_{\text{gas}} = 0.2$ bar and $p_{\text{gas}} = 2$ bar) are similar. The evening terminator was selected because of its intermediate temperature in the upper atmosphere at $p = 0.002$ bar. We use the full network as described in Sect. 3.1 for all simulations and start from chemical equilibrium calculated with GGchem.

To be able to compare gas-phase timescales to cloud formation timescales, we ran the VULCAN+ network (see Sect. 3.1) starting from solar-like atomic abundances for the $T_{\text{gas}}-p_{\text{gas}}$ points of the evening terminator. The resulting gas-phase concentrations of selected gas-phase species can be seen in Fig. 9. For all $T_{\text{gas}}-p_{\text{gas}}$ points, the concentrations of H_2O , TiO_2 , and SiO_2 quickly approach their stationary values ($\tau_{\text{chem}} < 1$ s). Their chemical timescale is highly pressure dependent and decreases for higher pressures. CH_4 and NH_3 on the other hand, still show significant differences for $t > 10^5$ s for all but the highest pressure ($p_{\text{gas}} = 2$ bar).

4.1. Time evolution of cloud formation

Our results for the cloud formation within HD 208458 b start from a chemical equilibrium gas-phase from which clouds are formed. These simulations therefore can give us an indication on the timescale of nucleation and bulk growth. The predicted cloud particle concentrations for most $T_{\text{gas}}-p_{\text{gas}}$ points of HD 209458 b quickly converge to stationary values ($\tau_{\text{nuc}} < 1$ s). The only exception is the sub-stellar point at $p_{\text{gas}} = 0.002$ bar where no cloud particles are predicted due to the high temperatures. Comparing the chemical timescales (see Fig. 9 or Tsai et al. 2018; Mendonça et al. 2018) to the nucleation timescale shows that nucleation happens on similar timescale as the chemical species with a shorter chemical timescale (e.g. H_2O , TiO_2 , SiO_2). The

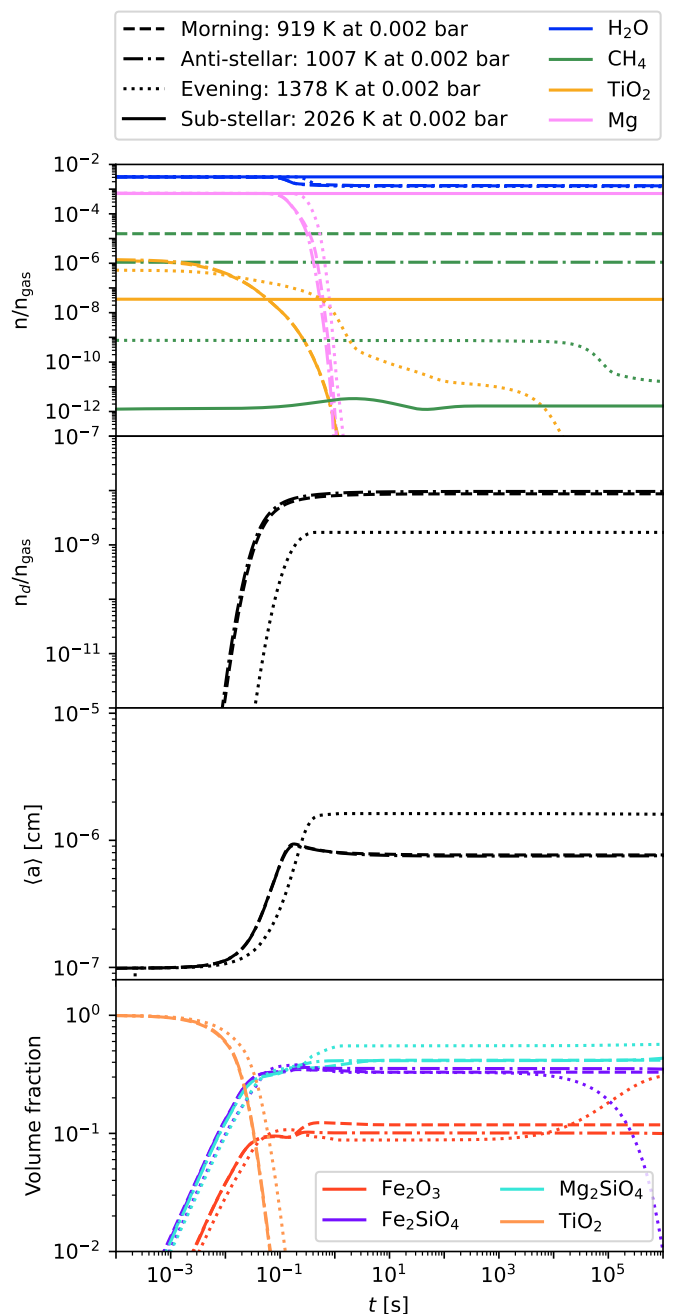


Fig. 7. Concentrations of selected gas-phase species (Top), cloud particle number density (Upper middle), mean cloud particle size (Lower middle), and selected volume fractions (Bottom) at the sub-stellar point, evening terminator, anti-stellar point and morning terminator at $p_{\text{gas}} = 0.002$ bar. The sub-stellar point does not form clouds.

$T_{\text{gas}}-p_{\text{gas}}$ points at $p_{\text{gas}} = 0.002$ bar, other than the sub-stellar point, show only a small temperature dependence of the predicted cloud particle concentrations and nucleation timescale. This is not unexpected for temperatures ranging from 919 K to 1378 K. We have shown that TiO_2 nucleation is roughly constant for this temperature range (see Sect. 3.3). Similarly, along the evening terminator we see a decrease in cloud particle concentrations consistent with the findings of Sect. 3.3. At $p_{\text{gas}} = 2$ bar within the evening terminator, the cloud particle concentration reaches only $n_d/n_{\text{gas}} \approx 10^{-22}$. The lower number of cloud particles results in larger cloud particles because the bulk growth ma-

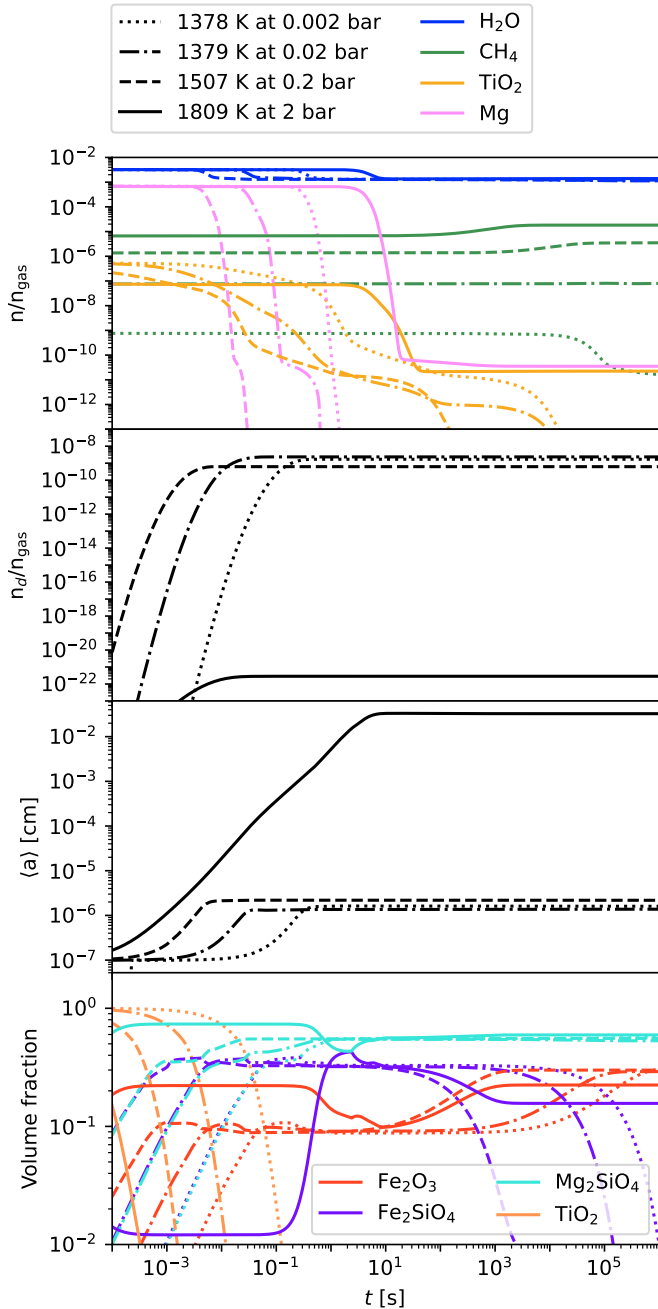


Fig. 8. Concentrations of selected gas-phase species (**Top**), cloud particle number density (**Upper middle**), mean cloud particle size (**Lower middle**), and selected volume fractions (**Bottom**) for logarithmically spaced pressures along the evening terminator.

material condense onto fewer particles (Helling et al. 2023). Hence, the average cloud particle size reaches up to 0.033 cm.

The peak in bulk growth closely follows the peak in nucleation and also approaches stationary values on timescales shorter than 1 second ($\tau_{\text{bulk}} < 1$ s). The exception to this is the evening terminator at $p_{\text{gas}} = 2$ bar. The cloud particles still grow at roughly the same speed, but since much more material is available per cloud particle, it takes longer to reach stationary values for the average cloud particle size.

In all cases, the volume fractions start out TiO_2 dominated. After bulk growth starts the cloud particles become considerably heterogeneous. In all cases, Mg_2SiO_4 becomes the domi-

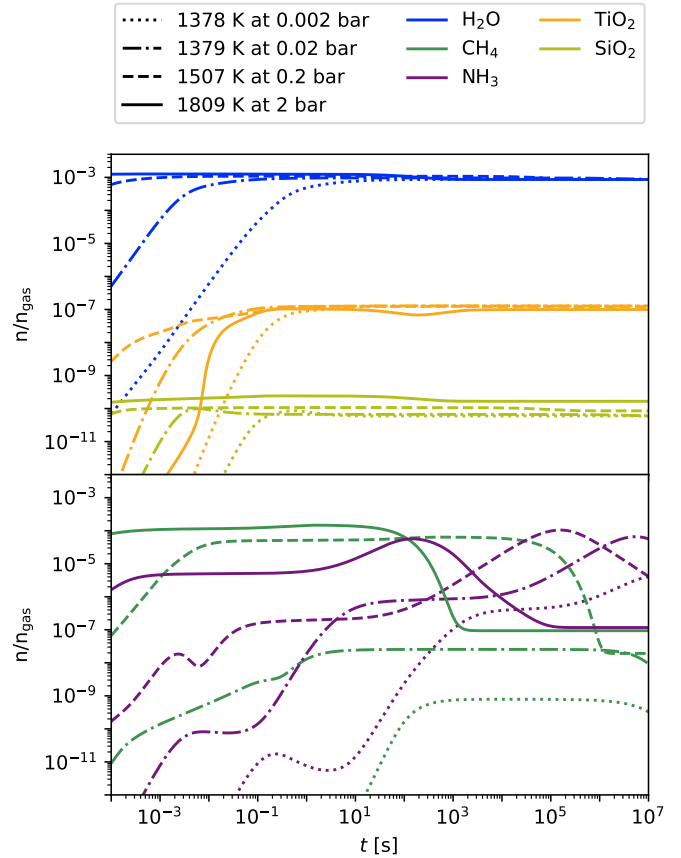


Fig. 9. Concentrations of selected gas-phase species along the evening terminator starting from solar-like atomic abundances.

nant bulk material and hence also the dominant Mg and Si bearing species. Around 0.1 to 1 second, a short increase in the average cloud particle size can be seen for the morning terminator and the anti-stellar point at $p_{\text{gas}} = 0.002$ bar. This size increase is caused by a temporary increase in $\text{SiO}[s]$, $\text{SiO}_2[s]$ and $\text{Fe}_2\text{SiO}_4[s]$ (see also Fig. F.1). Without the SiO-SiO₂ cycle the temporary peak of Fe_2SiO_4 still occurs. This temporary increase is likely a result of feedback between cloud formation and disequilibrium chemistry. Because the cloud formation is directly coupled to the gas phase via the reaction supersaturation ratio, temporary changes in the gas-phase chemistry can be caused by cloud formation and vice versa.

For the dominant Fe bearing species we see a switch from Fe_2SiO_4 to Fe_2O_3 for $t > 10^3$ s. These are similar timescales of CH_4 and NH_3 (see Fig. 9 or Tsai et al. 2018; Mendonça et al. 2018). It is important to note that the change in the dominant Fe bearing species is not related to the SiO-SiO₂ cycle. It still occurs even if $\text{SiO}[s]$ and $\text{SiO}_2[s]$ are not considered as bulk growth species. The timescale of the transition is highly pressure dependent and becomes shorter for higher pressures. Furthermore, the change in composition does not significantly affect the cloud particle size. Here it is important to note that our cloud formation formalism does not include any solid-to-solid composition changes. All changes happen via the gas-phase through bulk growth reactions as described in Sect. 2.5.

Helling & Woitke (2006) analysed the timescales of cloud formation with a similar cloud model as used in this work. In contrast to our work, the gas-phase is assumed to be in equilibrium (and depleted by cloud formation), MCNT is used to

describe nucleation, and fewer surface reactions are used. The nucleation and bulk growth timescales they find are similar to ours ($\tau_{\text{nuc}} < 1$ s and $\tau_{\text{bulk}} < 1$ s). Coupling gas-phase chemistry and cloud formation does not seem to impact these timescales. However, secondary effects like the change in the dominant Fe-bearing species and the SiO-SiO₂ cycle only appear once gas-phase chemistry and cloud formation are fully coupled.

Powell et al. (2018) also analysed the timescales of cloud formation using a diffusive approach. Their rates are limited by the time it takes for the key species to diffuse to the cloud particle. They calculate their timescales as the number density of cloud particles divided by the influx of new cloud particles once a stationary solution has been reached. Consequently, their growth and nucleation timescales for TiO₂ are larger than ours ($\tau_{\text{nuc}} > 10$ s and $\tau_{\text{bulk}} > 10$ s).

4.2. Comparison to dynamical processes

To find whether cloud formation happens in disequilibrium or is affected by disequilibrium chemistry, we compare our results to different dynamical processes.

4.2.1. Gravitational settling

Cloud particles in exoplanet atmospheres gravitationally settle over time. Whether gravitational settling timescales are faster than cloud formation timescales depends on many factors such as the bulk growth speed, bulk growth material replenishment, and the frictional force of cloud particles within the atmosphere (Woitke & Helling 2003). For smaller particles ($\langle a \rangle < 10^{-4}$ cm), growth is generally more efficient than gravitational settling (Woitke & Helling 2003; Powell et al. 2018). However, if the condition favour larger particles and gravitational settling becomes more efficient "cold traps" can occur (Parmentier et al. 2013, 2016; Powell et al. 2018) where most cloud material is concentrated at the cloud base.

Comparing our cloud particle number densities and average radii to Powell et al. (2018) reveals differences that can be explained by gravitational settling and replenishment. In contrast to our work, they generally predict less and larger cloud particles. Settling removes cloud particles from the atmosphere thus leading to less particles. The replenished material then condenses onto already existing particles. Since fewer particles are present, they become larger. The exception to this is the evening terminator at $p_{\text{gas}} = 2$ bar. Here, nucleation is so inefficient that we predict very large cloud particles ($\langle a \rangle = 0.033$ cm). However, these particles would quickly settle down and they are unlikely to persist in a 1D model.

4.2.2. Vertical and horizontal transport

Quenching occurs when the chemical timescale τ_{chem} [s] becomes larger than the vertical mixing timescale τ_{dyn} [s] (Moses 2014). In low density environments, chemical timescales typically become longer (Tsai et al. 2018) and dynamical timescales typically become smaller (Parmentier et al. 2013). Therefore, quenching becomes more relevant in the upper atmosphere of exoplanets (Baeyens et al. 2021). Typical vertical mixing timescales are between 10^3 s $< \tau_{\text{dyn}} < 10^7$ s (Agundez et al. 2014; Drummond et al. 2018; Baeyens et al. 2021). Our results show that nucleation happens on much shorter timescales than this ($\tau_{\text{nuc}} < 1$ s) and is therefore expected to be less affected by quenching. The cloud particle composition on the other hand

changes on longer timescales which are similar to the chemical timescales of CH₄ and NH₃. Both CH₄ and NH₃ are known to be gas-phase species affected by quenching (Moses et al. 2011). Therefore, the cloud particle composition might be susceptible to quenching as well.

Similar to the vertical timescale, one can compare the nucleation and bulk growth timescales to the horizontal mixing timescales which consists of the latitudinal timescale and the longitudinal timescale. Mendonça et al. (2018) analysed⁸ WASP-43 b and found that latitudinal mixing happens on similar timescales as the vertical timescale. Longitudinal mixing on the other hand can be orders of magnitude shorter. This is mostly due to the strong equatorial wind jets. In their analysis, all (longitudinal, latitudinal and vertical) mixing timescales are well above 10^3 s $> \tau_{\text{dyn}}$. Therefore, similar to quenching, nucleation and the peak in bulk growth might be less affected by horizontal mixing. The cloud particle composition on the other hand might be impacted.

4.2.3. Stellar Flares

If periodic effects disturb the chemical abundances, the relaxation timescale τ_{relax} indicates how quickly the chemical abundances return back to pre-disruption values. An example for an effect that temporarily impacts chemistry are stellar flares. They periodically enhance the radiation received by a planet and cause chemical disequilibrium through photochemistry (Tilley et al. 2019; Louca et al. 2022). The chemical relaxation timescale after a stellar flare event can be on the order of hours ($\tau_{\text{relax}} > 10^3$ s; Konings et al. 2022). In the chemical relaxation scheme (Smith 1998; Cooper & Showman 2006; Kawashima & Min 2021) the relaxation timescale is given by the chemical timescale. This scheme typically also finds relaxation timescales of $\tau_{\text{relax}} > 10^3$ s for CH₄ and NH₃ (see Fig. 9 or Tsai et al. 2018; Mendonça et al. 2018). Nucleation and the peak in bulk growth occur on much shorter timescales than this and therefore can adjust to the temporary chemical disequilibrium. The cloud particle composition on the other hand takes longer to transition and might not adjust to the temporary chemical disequilibrium.

5. Summary

We established a fully kinetic cloud formation description combining disequilibrium chemistry, kinetic nucleation and bulk growth through condensation and surface reactions. The kinetic gas-phase chemistry network for this study was based on the "NCHO thermo network" of VULCAN. This network was expanded with Ti (and Si) reactions to connect the gas-phase chemistry with the kinetic nucleation of TiO₂. We considered TiO₂ polymer nucleation using cluster data up to cluster size $N = 15$. For the bulk material, we considered TiO₂[s], Al₂O₃[s], SiO[s], SiO₂[s], Mg₂SiO₄[s], FeO[s], FeS[s], Fe₂O₃[s], and Fe₂SiO₄[s]. These materials can grow through 59 bulk growth reactions.

The kinetic polymer nucleation of TiO₂ indicates a similar temperature and pressure dependence as previous non-classical studies. We tested different maximum cluster sizes between $N_{\text{max}} = 7$ and $N_{\text{max}} = 15$ and found differences of the predicted cloud particle number density within a factor of 2. For further investigations, thermodynamic data of larger TiO₂ clusters is required. Overall, our results suggest that kinetic nucleation is a

⁸ WASP-43 b ($T_{\text{eq}} = 1400$ K) is a hot Jupiter with a slightly colder equilibrium temperature than HD 209458 b ($T_{\text{eq}} = 1500$ K) (Helling et al. 2021).

viable alternative to classical nucleation theory if the cluster data of the nucleating species is available. The required cluster sizes depend on the nucleating species.

The fully kinetic description of surface reactions resulted in a SiO-SiO₂ catalytic cycle that dissociates H₂ into 2 H. The increase in atomic hydrogen can reduce the CH₄ abundance by over an order of magnitude. If this catalytic cycle occurs in exoplanet atmospheres remains to be seen.

We simulated the chemistry of various $T_{\text{gas}}-p_{\text{gas}}$ points within the atmosphere of HD 209458 b. For all $T_{\text{gas}}-p_{\text{gas}}$ points, except the sub-stellar point, nucleation and bulk growth occurred. In all cases were nucleation occurred, nucleation and bulk growth reached a stationary behavior within 1 s. A comparison to the timescales of quenching and chemical relaxation showed that nucleation can happen on much shorter timescales. Hence, our work confirms that the assumption of localised nucleation is generally justified in exoplanet atmospheres. For the cloud particle composition on the other hand, we found changes on the timescale larger than 10³ seconds. This indicates that the composition of cloud particles can be susceptible to quenching.

Acknowledgements. S.K. H.L.M., Ch.H., and L.D. acknowledge funding from the European Union H2020-MSCA-ITN-2019 under grant agreement no. 860470 (CHAMELEON). N.B acknowledges financial support from the Austrian Academy of Sciences.

References

- Ackerman, A. S. & Marley, M. S. 2001, *ApJ*, 556, 872
- Agundez, M., Parmentier, V., Venot, O., Hersant, F., & Selsis, F. 2014, *A&A*, 564, A73
- Allard, F., Hauschildt, P. H., Alexander, D. R., Tamanai, A., & Schweitzer, A. 2001, *ApJ*, 556, 357
- Andersson, S., Gobrecht, D., & Valero, R. 2023, *Front. astron. space sci.*, 10
- Asplund, M., Grevesse, N., Sauval, A. J., & Scott, P. 2009, *ARA&A*, 47, 481
- Baeyens, R., Decin, L., Carone, L., et al. 2021, *MNRAS*, 505, 5603
- Bakes, E. L. O., Lebonnois, S., Bauschlicher, C. W., & McKay, C. P. 2003, *Icarus*, 161, 468
- Barman, T. S., Konopacky, Q. M., Macintosh, B., & Marois, C. 2015, *ApJ*, 804, 61
- Barth, P., Helling, Ch., Stüeken, E. E., et al. 2021, *MNRAS*, 502, 6201
- Baxter, C., Désert, J.-M., Tsai, S.-M., et al. 2021, *A&A*, 648, A127
- Bean, J. L., Miller-Ricci Kempton, E., & Homeier, D. 2010, *Nature*, 468, 669
- Borsa, F., Fossati, L., Koskinen, T., Young, M. E., & Shulyak, D. 2022, *Nat Astron*, 6, 226
- Boulangier, J., Gobrecht, D., Decin, L., de Koter, A., & Yates, J. 2019, *MNRAS*, 489, 4890
- Bromley, S. T., Martín, J. C. G., & C. Plane, J. M. 2016, *PCCP*, 18, 26913
- Campbell, M. L. & McClean, R. E. 1993, *J. Phys. Chem.*, 97, 7942
- Chadney, J. M., Koskinen, T. T., Galand, M., Unruh, Y. C., & Sanz-Forcada, J. 2017, *A&A*, 608, A75
- Chang, C., Patzer, A. B. C., Kegel, W. H., & Chandra, S. 2013, *Astrophys Space Sci*, 347, 315
- Chang, C., Patzer, A. B. C., Sedlmayr, E., & Sülzle, D. 2005, *Phys. Rev. B*, 72, 235402
- Chiodo, L., Salazar, M., Romero, A. H., et al. 2011, *J. Chem. Phys.*, 135, 244704
- Cooper, C. S. & Showman, A. P. 2006, *ApJ*, 649, 1048
- Courtin, R., Wagnener, R., McKay, C. P., et al. 1991, *Icarus*, 90, 43
- Crossfield, I. J. M. 2015, *PASP*, 127, 941
- Crowther, P. A. 2003, *Ap&SS*, 285, 677
- Decin, L., Cherchneff, I., Hony, S., et al. 2008, *A&A*, 480, 431
- Decin, L., Danilovich, T., Gobrecht, D., et al. 2018, *ApJ*, 855, 113
- Decin, L., Richards, A. M. S., Waters, L. B. F. M., et al. 2017, *A&A*, 608, A55
- Demory, B.-O., Wit, J. d., Lewis, N., et al. 2013, *ApJL*, 776, L25
- Dishoeck, E. F. v. 2014, *Faraday Discuss.*, 168, 9
- Domink, C., Sedlmayr, E., & Gail, H.-P. 1993, *A&A*, 277, 578
- Drummond, B., Mayne, N. J., Manners, J., et al. 2018, *ApJL*, 855, L31
- Espinoza, N., Rackham, B. V., Jordán, A., et al. 2019, *MNRAS*, 482, 2065
- Ferraro, A. S. & Gail, H.-P. 2006, *A&A*, 447, 553
- Fleischer, A. J., Winters, J. M., & Sedlmayr, E. 1999, *Asymptotic Giant Branch Stars*, IAU Symposium #191, 191, 187
- Gail, H.-P., Keller, R., & Sedlmayr, E. 1984, *A&A*, 133, 320
- Gail, H.-P. & Sedlmayr, E. 1986, *A&A*, 166, 225
- Gail, H.-P. & Sedlmayr, E. 1988, *A&A*, 206, 153
- Gauger, A., Gail, H. P., & Sedlmayr, E. 1990, *A&A*, 235, 345
- Gobrecht, D., Cherchneff, I., Sarangi, A., Plane, J. M. C., & Bromley, S. T. 2016, *A&A*, 585, A6
- Gobrecht, D., Plane, J. M. C., Bromley, S. T., et al. 2022, *A&A*, 658, A167
- Goumans, T. P. M. & Bromley, S. T. 2013, *Phil. Trans. R. Soc. A*, 371, 20110580
- Guillot, T., Fletcher, L. N., Helled, R., et al. 2022, *Giant Planets from the Inside-Out*, chapter submitted to *Protostars and Planets VII*
- Guilluy, G., Giacobbe, P., Carleo, I., et al. 2022, *A&A*, 665, A104
- Guilluy, G., Sozzetti, A., Brogi, M., et al. 2019, *A&A*, 625, A107
- Helling, Ch. & Fomins, A. 2013, *Phil. Trans. R. Soc. A*, 371, 20110581
- Helling, Ch., Gourbin, P., Woitke, P., & Parmentier, V. 2019, *A&A*, 626, A133
- Helling, Ch., Klein, R., Woitke, P., Nowak, U., & Sedlmayr, E. 2004, *A&A*, 423, 657
- Helling, Ch., Lewis, D., Samra, D., et al. 2021, *A&A*, 649, A44
- Helling, Ch., Oevermann, M., Lüttke, M. J. H., Klein, R., & Sedlmayr, E. 2001, *A&A*, 376, 194
- Helling, Ch. & Rimmer, P. B. 2019, *Philosophical Transactions of the Royal Society A: Mathematical, Physical and Engineering Sciences*, 377, 20180398
- Helling, Ch., Samra, D., Lewis, D., et al. 2023, *A&A*, 671, A122
- Helling, Ch., Tootill, D., Woitke, P., & Lee, E. K. H. 2017, *A&A*, 603, A123
- Helling, Ch. & Woitke, P. 2006, *A&A*, 455, 325
- Helling, Ch., Woitke, P., & Thi, W.-F. 2008, *A&A*, 485, 547
- Herbst, E. 2014, *Phys. Chem. Chem. Phys.*, 16, 3344
- Herbst, E. 2017, *International Reviews in Physical Chemistry*, 36, 287
- Highberger, J. L., Savage, C., Biegging, J. H., & Ziurys, L. M. 2001, *ApJ*, 562, 790
- Higuchi, Y., Fukuda, Y., Fujita, Y., Yamakita, N., & Imajo, T. 2008, *Chemical Physics Letters*, 452, 245
- Hindmarsh, A. C. 1983, *Scientific Computing*, 55
- Hobbs, R., Shorttle, O., & Madhusudhan, N. 2022, *MNRAS*, 516, 1032
- Hobbs, R., Shorttle, O., Madhusudhan, N., & Rimmer, P. 2019, *MNRAS*, 487, 2242
- Hoeymakers, H. J., Ehrenreich, D., Heng, K., et al. 2018a, *Nature*, 560, 453
- Hoeymakers, H. J., Schwarz, H., Snellen, I. A. G., et al. 2018b, *A&A*, 617, A144
- Hoeymakers, H. J., Seidel, J. V., Pino, L., et al. 2020, *A&A*, 641, A123
- Hollenbach, D. & Salpeter, E. E. 1971, *ApJ*, 163, 155
- Huang, J., Seager, S., Petkowski, J. J., Zhan, Z., & Ranjan, S. 2022, *ApJ*, 933, 6
- Höfner, S. 2009, *Proceedings of the ASP Conference Series, Cosmic Dust - Near and Far ed Th. Henning, E. Gruen, J. Steinacker*, 414, 3
- Javoy, S., Naudet, V., Abid, S., & Paillard, C. E. 2003, *Exp. Therm. Fluid Sci*, 27, 371
- Kammerer, J., Lacour, S., Stolker, T., et al. 2021, *A&A*, 652, A57
- Kawashima, Y. & Min, M. 2021, *A&A*, 656, A90
- Kempton, E. M.-R., Bean, J. L., & Parmentier, V. 2017, *ApJL*, 845, L20
- Khouri, T., Maercker, M., Waters, L. B. F. M., et al. 2016, *A&A*, 591, A70
- Kiefer, S., Gobrecht, D., Decin, L., & Helling, Ch. 2023, *A&A*, 671, A169
- Kok, R. J. d., Brogi, M., Snellen, I. a. G., et al. 2013, *A&A*, 554, A82
- Konings, T., Baeyens, R., & Decin, L. 2022, *A&A*, 667, A15
- Kreidberg, L., Bean, J. L., Désert, J.-M., et al. 2014, *Nature*, 505, 69
- Köhn, C., Helling, Ch., Enghoff, M. B., et al. 2021, *A&A*, 654, A120
- Lasserus, M., Schnedlitz, M., Messner, R., et al. 2019, *Chem. Sci.*, 10, 3473
- Lau, R. M., Hankins, M. J., Han, Y., et al. 2022, *Nat Astron*, 6, 1308
- Lazzati, D. 2008, *MNRAS*, 384, 165
- Lebonnois, S., Bakes, E. L. O., & McKay, C. P. 2003, *Icarus*, 161, 474
- Lee, E., Casewell, S. L., Chubb, K. L., et al. 2020, *MNRAS*, 496, 4674
- Lee, E. K. H., Helling, Ch., Giles, H., & Bromley, S. T. 2015, *A&A*, 575, A11
- Lee, E. K. H., Tsai, S.-M., Hammond, M., & Tan, X. 2023, *A&A*, 672, A110
- Libby-Roberts, J. E., Berta-Thompson, Z. K., Diamond-Lowe, H., et al. 2022, *AJ*, 164, 59
- Louca, A. J., Miguel, Y., Tsai, S.-M., et al. 2022, *MNRAS*, stac1220
- Lundqvist, M. J., Nilsing, M., Persson, P., & Lunell, S. 2006, *Int. J. Quantum Chem.*, 106, 3214
- Maire, A.-L., Baudino, J.-L., Desidera, S., et al. 2020, *A&A*, 633, L2
- McElroy, D., Walsh, C., Markwick, A. J., et al. 2013, *A&A*, 550, A36
- Mendonça, J. M., Tsai, S.-m., Malik, M., Grimm, S. L., & Heng, K. 2018, *ApJ*, 869, 107
- Molaverdikhani, K., Henning, T., & Mollière, P. 2019, *ApJ*, 883, 194
- Molaverdikhani, K., Henning, T., & Mollière, P. 2020, *ApJ*, 899, 53
- Moses, J. I. 2014, *Philos. Trans. Royal Soc. A PHILOS T R SOC A*, 372, 20130073
- Moses, J. I., Fouchet, T., Bézard, B., et al. 2005, *J. Geophys. Res. Planets*, 110
- Moses, J. I., Visscher, C., Fortney, J. J., et al. 2011, *ApJ*, 737, 15
- Niculescu-Duvaz, M., Barlow, M. J., Bevan, A., et al. 2022, *MNRAS*, 515, 4302
- Parmentier, V., Fortney, J. J., Showman, A. P., Morley, C., & Marley, M. S. 2016, *ApJ*, 828, 22
- Parmentier, V., Showman, A. P., & Lian, Y. 2013, *A&A*, 558, A91
- Patzer, A. B. C., Chang, C., & Sülzle, D. 2014, *Chemical Physics Letters*, 612, 39
- Patzer, A. B. C., Gauger, A., & Sedlmayr, E. 1998, *A&A*, 337, 847

- Peters, B. 2017, in *Reaction Rate Theory and Rare Events Simulations*, ed. B. Peters (Amsterdam: Elsevier), 147–156
- Plane, J. M. C. 2013, *Philos. Trans. Royal Soc. A PHILOS T R SOC A*, 371, 20120335
- Plane, J. M. C. & Robertson, S. 2022, *Faraday Discuss.*, 238, 461, publisher: Royal Society of Chemistry
- Powell, D., Zhang, X., Gao, P., & Parmentier, V. 2018, *ApJ*, 860, 18
- Prinoth, B., Hoiemakers, H. J., Kitzmann, D., et al. 2022, *Nat Astron*, 6, 449
- Qu, Z.-w. & Kroes, G.-J. 2006, *J. Phys. Chem. B*, 110, 8998
- Radhakrishnan, K. & Hindmarsh, A. C. 1993, *NASA Reference Publication*, 19940030753
- Rimmer, P. B. & Helling, Ch. 2013, *ApJ*, 774, 108
- Rimmer, P. B. & Helling, Ch. 2016, *ApJS*, 224, 9
- Ritter, D. & Weisshaar, J. C. 2002, *ACS Publications*, 93, 1576
- Roman, M. & Rauscher, E. 2017, *ApJ*, 850, 17
- Roman, M. T., Kempton, E. M.-R., Rauscher, E., et al. 2021, *ApJ*, 908, 101
- Sabri, T., Gavilan, L., Jäger, C., et al. 2013, *The Astrophysical Journal*, 780, 180, publisher: The American Astronomical Society
- Sande, M. V. d. & Millar, T. J. 2019, *ApJ*, 873, 36
- Schneider, A. D., Carone, L., Decin, L., et al. 2022, *A&A*, 664, A56
- Sekine, Y., Imanaka, H., Matsui, T., et al. 2008, *Icarus*, 194, 186
- Sindel, J. P., Gobrecht, D., Helling, Ch., & Decin, L. 2022, *A&A*, 668, A35
- Smith, M. D. 1998, *Icarus*, 132, 176
- Smolders, K., Acke, B., Verhoelst, T., et al. 2010, *A&A*, 514, L1
- Spyratos, P., Nikolov, N., Southworth, J., et al. 2021, *MNRAS*, 506, 2853
- Stock, J. W., Kitzmann, D., Patzer, A. B. C., & Sedlmayr, E. 2018, *MNRAS*, 479, 865
- Swain, M. R., Tinetti, G., Vasisht, G., et al. 2009, *ApJ*, 704, 1616
- Thompson, M. A., Krissansen-Totton, J., Wogan, N., Telus, M., & Fortney, J. J. 2022, *Proceedings of the National Academy of Sciences*, 119, e2117933119
- Tilley, M. A., Segura, A., Meadows, V. S., Hawley, S., & Davenport, J. 2019, *Astrobiology*, 19, 64
- Tinyanont, S., Kasliwal, M. M., Krafton, K., et al. 2019, *ApJ*, 873, 127
- Toublanc, D., Parisot, J. P., Brillet, J., et al. 1995, *Icarus*, 113, 2
- Tsai, S.-M., Kitzmann, D., Lyons, J. R., et al. 2018, *ApJ*, 862, 31
- Tsai, S.-M., Lee, E. K. H., & Pierrehumbert, R. 2022, *A&A*, 664, A82
- Tsai, S.-M., Lee, E. K. H., Powell, D., et al. 2023, *Nature*, 617, 483
- Tsai, S.-M., Lyons, J. R., Grosheintz, L., et al. 2017, *ApJS*, 228, 20
- Tsai, S.-M., Malik, M., Kitzmann, D., et al. 2021, *ApJ*, 923, 264
- Venot, O. & Agúndez, M. 2015, *Exp Astron*, 40, 469
- Venot, O., Cavalié, T., Bounaceur, R., et al. 2020, *A&A*, 634, A78
- Venot, O., Drummond, B., Miguel, Y., et al. 2018, *Exp Astron*, 46, 101
- Venot, O., Hébrard, E., Agúndez, M., et al. 2012, *A&A*, 546, A43
- Ward-Duong, K., Patience, J., Follette, K., et al. 2020, *ApJ*, 161, 5
- Webber, M. W., Lewis, N. K., Marley, M., et al. 2015, *ApJ*, 804, 94
- Williams, D. A. 2005, *Journal of Physics: Conference Series*, 6, 1
- Williams, P. M., van der Hucht, K. A., & The, P. S. 1987, *A&A*, 182, 91
- Woitke, P. & Helling, Ch. 2003, *A&A*, 399, 297
- Woitke, P. & Helling, Ch. 2021, *Astrophysics Source Code Library*, ascl:2104.018
- Yung, Y. L., Allen, M., & Pinto, J. P. 1984, *The Astrophysical Journal Supplement Series*, 55, 465
- Zhai, H.-J. & Wang, L.-S. 2007, *J. Am. Chem. Soc.*, 129, 3022
- Zhang, X., Wang, X., Sai, H., et al. 2022, *MNRAS*, 509, 2013

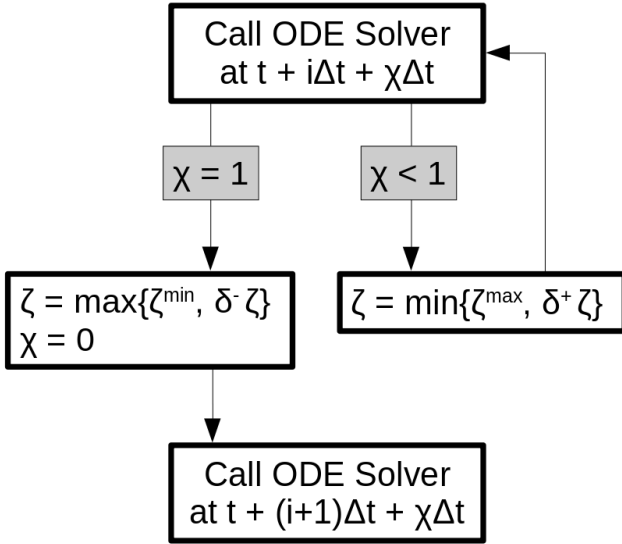


Fig. A.1. Dynamic tolerances scheme for the ODE solver.

Appendix A: Numerical solver

The chemical kinetic network can be described as an ordinary differential equation (ODE). Therefore, a fast and accurate ODE solver is required. Similar to other works (e.g. Agundez et al. 2014; Rimmer & Helling 2016; Molaverdikhani et al. 2019; Baeyens et al. 2021), we chose DLSODES from ODEPACK (Hindmarsh 1983; Radhakrishnan & Hindmarsh 1993).

Combining chemistry, nucleation and bulk growth through condensation and surface reactions results in a stiff ODE system, especially during the onset of nucleation and the onset of bulk growth. To prevent the solver from getting stuck, we introduce dynamic tolerances. During the iteration, the solver tries to compute a given time step Δt with a given relative tolerance ζ_{rel} and a given absolute tolerance ζ_{abs} . If the solver only reaches a percentage $\chi < 1$ of the time-step, ζ_{rel} and ζ_{abs} are increased by a factor of δ_{rel}^+ and δ_{abs}^+ , respectively. If the solver reaches the full time step $\chi = 1$, the relative and absolute tolerances are decreased by a factor of δ_{rel}^- and δ_{abs}^- , respectively. To ensure sufficient precision of the ODE, the tolerances have an upper limit $\zeta_{\text{rel}}^{\text{max}}$ and $\zeta_{\text{abs}}^{\text{max}}$, and a lower limit $\zeta_{\text{rel}}^{\text{min}}$ and $\zeta_{\text{abs}}^{\text{min}}$, respectively. The schematics of the algorithm is show in Fig. A.1. In this paper, the following values are used:

$$\zeta_{\text{rel}}^{\text{max}} = 10^{-3} \quad (\text{A.1})$$

$$\zeta_{\text{abs}}^{\text{max}} = 10^{-40} \quad (\text{A.2})$$

$$\zeta_{\text{rel}}^{\text{min}} = 10^{-9} \quad (\text{A.3})$$

$$\zeta_{\text{abs}}^{\text{min}} = 10^{-60} \quad (\text{A.4})$$

$$\delta_{\text{rel}}^- = \delta_{\text{abs}}^- = 0.1 \quad (\text{A.5})$$

$$\delta_{\text{rel}}^+ = \delta_{\text{abs}}^+ = 1.1 \quad (\text{A.6})$$

The starting tolerance is always equal to the minimum tolerance and was selected depending on the simulation.

Appendix B: GGchem

We consider the following species in our chemical equilibrium calculations done with GGchem: OH, H₂, H₂O, H, O, CH, C, CH₂, CH₃, CH₄, C₂, C₂H₂, C₂H, C₂H₃, C₂H₄, C₂H₅, C₂H₆, CO, CO₂, CH₂OH, H₂CO, HCO, CH₃O, CH₃OH, CH₃CO, O₂,

H₂CCO, HCCO, N, NH, CN, HCN, NO, NH₂, N₂, NH₃, N₂H₂, N₂H, N₂H₃, N₂H₄, HNO, H₂CN, HNCO, NO₂, N₂O, C₄H₂, CH₂NH₂, CH₂NH, CH₃NH₂, CH₃CHO, HNO₂, NCO, HO₂, H₂O₂, HC₃N, CH₃CN, CH₂CN, C₂H₃CN, C₃H₃, C₃H₂, C₃H₄, C₄H₃, C₄H₅, C₆H₆, C₆H₅, (O)₁, (CH₂)₁, (N₂)_D, He, Ti, TiO, SO₂, SO, TiO₂, SiO⁺, Si⁺, SiH⁺, H⁻, Si, HF, SiF⁺, He⁺, SiO₂, Na, Na⁺, SiO, HCO⁺, P⁺, P, S⁺, S, e⁻, Fe, Fe⁺, F, (TiO₂)₂, (TiO₂)₃, (TiO₂)₄, (TiO₂)₅, (TiO₂)₆, (TiO₂)₇, (TiO₂)₈, (TiO₂)₉, (TiO₂)₁₀, (TiO₂)₁₁, (TiO₂)₁₂, (TiO₂)₁₃, (TiO₂)₁₄, (TiO₂)₁₅, Mg, Al, Ca, Cl, FeO₂, Al₂O₃, AlH₂, AlH₃, Al(OH)₂, Al(OH)₃, H₂S₂, F₂, Mg₂, Al₂, Si₂, S₂, Cl₂, MgH, AlH, SiH, HS, HCl, CaH, TiH, FeH, CF, SiC, CS, CCl, FN, AlN, SiN, SN, NCl, TiN, FO, MgO, AlO, ClO, CaO, FeO, MgF, AlF, SiF, SF, CaF, MgS, AlS, SiS, CaS, TiS, MgCl, AlCl, SiCl, CaCl, FeCl, AlClF, AlClF₂, AlOCl, AlCl₂, AlCl₂F, AlCl₃, AlOF, AlF₂, AlF₂O, AlF₃, AlOH, HAIO, AlO₂H, AlO₂, Al₂Cl₆, (AlF₃)₂, Al₂O, Al₂O₂, AlC, CFCIO, CClF₃, CCIN, CClO, CCl₂, CCl₂F₂, COCl₂, CCl₃, CCl₃F, CCl₄, CFN, CFO, CF₂, CF₂O, CF₃, CF₄, CF₄O, CF₈S, CHCl, CHCl₃, CHF, CHFO, CHF₃, CHNO, CH₂Cl₂, CH₂ClF, CH₂F₂, CH₃Cl, CH₃F, CNO, CNN, NCN, COS, CS₂, Si₂C, C₂Cl₂, C₂Cl₄, C₂Cl₆, C₂F₂, C₂F₃N, C₂F₄, C₂F₆, C₂HCl, C₂HF, C₂H₄O, C₂N, C₂N₂, SiC₂, C₂O, C₃, C₃O₂, C₄, C₄N₂, C₅, Fe(CO)₅, CaCl₂, CaF₂, CaOH, Ca(OH)₂, Ca₂, ClF, MgClF, ClFO₂S, ClFO₃, ClF₃, ClF₃Si, ClF₅, ClF₅S, CHClF₂, CHCl₂F, OHCl, SiH₃Cl, NOCl, NO₂Cl, TiOCl, ClO₂, ClO₃, SCl, ClS₂, TiCl, FeCl₂, SiH₂Cl₂, MgCl₂, ClOCl, ClClO, TiOCl₂, ClO₂Cl, ClOClO, SO₂Cl₂, SCl₂, SiCl₂, TiCl₂, SiFCl₃, FeCl₃, SiHCl₃, SiCl₃, TiCl₃, Fe₂Cl₄, Mg₂Cl₄, SiCl₄, TiCl₄, (FeCl₃)₂, FeF, FHO, FHO₃S, SiH₃F, FNO, FNO₂, FNO₃, TiOF, OFO, FOO, TiF, FeF₂, H₂F₂, SiH₂F₂, MgF₂, F₂N, F₂N₂(cis), F₂N₂(trans), F₂O, F₂OS, SiOF₂, TiOF₂, F₂O₂, F₂O₂S, SF₂, FSSF, F₂S₂, SiF₂, TiF₂, FeF₃, SiHF₃, F₃H₃, NF₃, NOF₃, SF₃, SiF₃, TiF₃, F₄H₄, Mg₂F₄, N₂F₄, SF₄, SiF₄, TiF₄, F₃H₅, SF₅, F₆H₆, SF₆, F₇H₇, F₁₀S₂, Fe(OH)₂, FeS, MgOH, HONO, HNO₃, Mg(OH)₂, H₂SO₄, H₂S, SiH₄, MgN, NO₃, Si₂N, N₂O₃, N₂O₄, N₂O₅, N₃, S₂O, O₃, SO₃, S₃, S₄, S₅, S₆, S₇, S₈, Si₃, TiC, Si(CH₃)₄, SiCH₃Cl₃, SiH₂, SiH₃, TiC₂, C₃H, Si₂C₂, and TiC₄.

Appendix C: Al₂O₃ nucleation

To calculate the nucleation rate of potential nucleation species, thermodynamic data of their clusters needs to be available. With TiO₂, we are in the fortunate position of having data available up to N = 15 (Sindel et al. 2022). For Al₂O₃ we only have data up to N = 10 from Gobrecht et al. (2022). They also derived a detailed chemical kinetics network up to (Al₂O₃)₄, including a small C-H-O network for the gas-phase.

Similar as in Sect. 3.3, we calculated the predicted cloud particle number densities and nucleation rate of Al₂O₃ using $5 \leq N_{\text{max}} \leq 10$, but the results were inconclusive and no stable nucleation behaviour was found. Neither the cloud particle number density nor the nucleation rate showed any clear trends with N_{max}. A possible explanation for this non-convergence could be that the thermally stable cluster is (much) larger than N_{max} = 10 or that Al₂O₃ does not follow homogeneous nucleation. More studies on the formation of Al₂O₃ clusters is required to model the kinetic nucleation of Al₂O₃.

Appendix D: Comparing chemical networks

The cloud formation model described in this paper can be combined with any chemical kinetics network. Typically, the more extensive the network, the longer individual model runs take. In

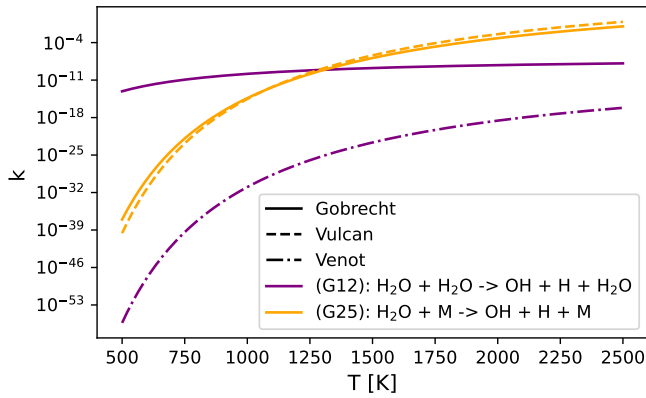


Fig. D.1. Comparison of reaction rate coefficients at $p_{\text{gas}} = 0.01$ bar. The unit of k is $[\text{cm}^3 \text{s}^{-1}]$ for G12 and $[\text{s}^{-1}]$ for G25.

the development of this model, we first relied on a small C-H-O network taken from [Gobrecht et al. \(2022\)](#) (**Gobrecht**). Later we used the chemical network of [Tsai et al. \(2017\)](#) (**Vulcan**). Here, we compare the two networks.

Throughout this section, we reference multiple reactions from the chemical network of **Gobrecht** and use the following short hand:

- (G02): $\text{H}_2 + \text{H}_2 \rightarrow \text{H} + \text{H} + \text{H}_2$
- (G04): $\text{H}_2 + \text{H} \rightarrow \text{H} + \text{H} + \text{H}$
- (G06): $\text{H}_2 + \text{He} \rightarrow \text{H} + \text{H} + \text{He}$
- (G11): $\text{OH} + \text{H} + \text{H}_2\text{O} \rightarrow \text{H}_2\text{O} + \text{H}_2\text{O}$
- (G12): $\text{H}_2\text{O} + \text{H}_2\text{O} \rightarrow \text{OH} + \text{H} + \text{H}_2\text{O}$
- (G24): $\text{OH} + \text{H} + \text{M} \rightarrow \text{H}_2\text{O} + \text{M}$
- (G25): $\text{H}_2\text{O} + \text{M} \rightarrow \text{OH} + \text{H} + \text{M}$

Appendix D.1: Gobrecht vs Vulcan

With three exceptions, all reactions of **Gobrecht** can be found within **Vulcan**. The first exceptions are reaction G11 and G12, which do not appear in **Vulcan**. Especially reaction G12 has a significant impact on the concentration of all species. The reaction rate for G12, and its corresponding forward reaction G11, were derived in supersonic combustion chemistry experiments at $2790 \text{ K} < T < 3200 \text{ K}$ and $p = 250 \text{ kPa}$ ([Javoy et al. 2003](#)). A comparison with other chemical networks for exoplanet atmospheres revealed inconsistencies. Instead of G11 and G12, **Vulcan** only considers the reactions G24 and G25. These are similar reactions but with an arbitrary third body instead of H_2O . [Venot et al. \(2012\)](#) include reactions G11 and G12 but do not include G24 and G25. [Rimmer & Helling \(2016\)](#) do not consider any of the reactions G11, G12, G24, and G25. A comparison between the reaction rate coefficients of G12, and G25 can be seen in Fig. D.1.

The second difference between **Gobrecht** and **Vulcan** is the reaction G17. This reaction describes the radiative association of CO. Since we don't include any photochemical reactions in **Vulcan**, we also exclude this reaction for **Gobrecht**. From here on we call the collection of reactions corresponding to the network of **Gobrecht** without reactions G11, G12 and G17 the 'base' network.

The third difference is the description of H+H reactions. In **Gobrecht**, they are described as 3-body reactions with specific collision partners H, H_2 and He (G02, G04, and G06). In **Vulcan**, these reactions are described with a generic 3rd body M. We use

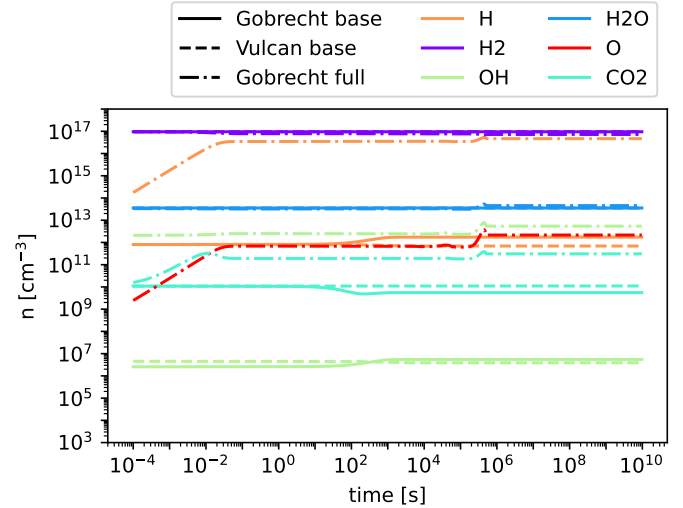


Fig. D.2. Comparison of the chemical network of **Gobrecht** and **Vulcan**.

each network's description of H+H reactions and don't adjust them.

Evaluating the base network for $T = 1300 \text{ K}$ and $p = 2000$ (Fig. D.2) once with reaction rates from **Gobrecht** and once with reaction rates from **Vulcan** only showed minor differences in CO_2 , OH, and H abundance. The differences are within expected offsets due to slightly different reaction rates and different Gibbs free energy values. The full network of **Gobrecht** still produced significantly different abundances.

Appendix D.2: Vulcan

We separate Vulcan's 780 reactions into three categories:

- **base**: The base **Vulcan** network as described in Appendix D.1.
- **won**: The reactions of the "NCHO thermo network" of **Vulcan** without Nitrogen species as reactant or product.
- **full**: The full "NCHO thermo network" of **Vulcan**.

Comparing the base and won network for $p_{\text{gas}} = 0.002$ bar and $T \in \{500 \text{ K}, 1300 \text{ K}, 2000 \text{ K}\}$ show little to no differences in H, O, OH, H_2 , H_2O , CO, and CO_2 number densities. Using the evaluation from Eq. 50 we find $P(A, \text{base}, \text{won}) < 10^{-3}$ for all of these species. Furthermore, also the deviations from chemical equilibrium as calculated with GGchem are minimal. Comparing the won and full network for $p_{\text{gas}} = 0.002$ bar and $T \in \{500 \text{ K}, 1300 \text{ K}, 2000 \text{ K}\}$ showed little to no differences in H, O, OH, H_2 , H_2O , CO, and CO_2 abundance. Using the evaluation from Eq. 50 we find $P(A, \text{won}, \text{full}) < 10^{-4}$ for all of these species.

Our results suggest that the VULCAN network could be used in the base or won configuration as well if a smaller network is desired. Especially the won network might prove useful since it includes the major species H_2O , CO, CO_2 , and CH_4 while having only 416 of the 780 reactions of the "NCHO thermo network" of **Vulcan**.

Appendix E: Data and additional plots

The Ti and Si reactions selected from [Boulangier et al. \(2019\)](#) and [Kiefer et al. \(2023\)](#) are listed in Table E.1. Some backward

reactions are derived using detailed balance with the following coefficients:

$$\text{EQS}_{18} = \exp\left(\frac{G_{\text{TiO}_2}^\ominus + G_{\text{H}}^\ominus - G_{\text{TiO}}^\ominus - G_{\text{OH}}^\ominus}{k_B T_{\text{gas}}}\right) \quad (\text{E.1})$$

$$\text{EQS}_{20} = \left(\frac{k_B T}{p^\ominus}\right) \exp\left(\frac{G_{\text{TiO}_2}^\ominus + G_{\text{TiO}_2}^\ominus - G_{(\text{TiO}_2)_2}^\ominus}{k_B T_{\text{gas}}}\right) \quad (\text{E.2})$$

$$\text{EQS}_{22} = \left(\frac{k_B T}{p^\ominus}\right) \exp\left(\frac{G_{(\text{TiO}_2)_2}^\ominus + G_{\text{TiO}_2}^\ominus - G_{(\text{TiO}_2)_3}^\ominus}{k_B T_{\text{gas}}}\right) \quad (\text{E.3})$$

$$\text{EQS}_{24} = \left(\frac{k_B T}{p^\ominus}\right) \exp\left(\frac{G_{(\text{TiO}_2)_3}^\ominus + G_{\text{TiO}_2}^\ominus - G_{(\text{TiO}_2)_4}^\ominus}{k_B T_{\text{gas}}}\right) \quad (\text{E.4})$$

$$\text{EQS}_{26} = \left(\frac{k_B T}{p^\ominus}\right) \exp\left(\frac{G_{(\text{TiO}_2)_2}^\ominus + G_{(\text{TiO}_2)_2}^\ominus - G_{(\text{TiO}_2)_4}^\ominus}{k_B T_{\text{gas}}}\right) \quad (\text{E.5})$$

The condensation reactions taken from [Helling et al. \(2019\)](#) and the fitting values for the reaction vapor coefficient (Eq. 43) are listed in Table E.2. In Fig. F.1, the volume fraction of all species from the simulations of Sect. 4 are shown.

Table E.1. Chemical reactions from Boulangier et al. (2019) and Kiefer et al. (2023) added to the "NCHO thermo network" of VULCAN.

Index (RNr)	Reaction	Reaction rate coefficient k	Origin
1	Ti + CO ₂ → TiO + CO	$7 \times 10^{-11} \exp(-14.9/(RT))$	(1)
2	TiO + CO → Ti + CO ₂	$7 \times 10^{-11} \exp(-14.9/(RT))$ EQR ₅₆₄	(1)
3	Ti + N ₂ O → TiO + N ₂	$1.74 \times 10^{-10} \exp(-14.3/(RT))$	(1)
4	TiO + N ₂ → Ti + N ₂ O	$1.74 \times 10^{-10} \exp(-14.3/(RT))$ EQR ₅₆₆	(1)
5	Ti + NO → TiO + N	$3.28 \times 10^{-11} \exp(-3.62/(RT))$	(1)
6	TiO + N → Ti + NO	$3.28 \times 10^{-11} \exp(-3.62/(RT))$ EQR ₅₆₅	(1)
7	Ti + NO ₂ → TiO + NO	9×10^{-11}	(1)
8	TiO + NO → Ti + NO ₂	9×10^{-11} EQR ₅₆₇	(1)
9	Ti + O ₂ → TiO + O	$1.69 \times 10^{-10} \exp(-11.6/(RT))$	(1)
10	TiO + O → Ti + O ₂	$1.69 \times 10^{-10} \exp(-11.6/(RT))$ EQR ₅₆₉	(1)
11	Ti + SO ₂ → TiO + SO	$1.7 \times 10^{-10} \exp(-2.66/(RT))$	(1)
12	TiO + SO → Ti + SO ₂	$1.7 \times 10^{-10} \exp(-2.66/(RT))$ EQR ₅₇₂	(1)
13	TiO + NO → TiO ₂ + N	2.2×10^{-12}	(4)
14	TiO ₂ + N → TiO + NO	2.2×10^{-12} EQR ₅₇₄	(4)
15	TiO + O ₂ → TiO ₂ + O	7.07×10^{-12}	(5)
16	TiO ₂ + O → TiO + O ₂	7.07×10^{-12} EQR ₅₇₀	(5)
17	TiO + OH → TiO ₂ + H	$2.07 \times 10^{-10} T^{0.39}$	(3)
18	TiO ₂ + H → TiO + OH	$2.07 \times 10^{-10} T^{0.39}$ EQS ₁₈	(0)
19	(TiO ₂) ₂ + M → TiO ₂ + TiO ₂ + M	$1.4 \times 10^{-4} \exp(-48870/T)$	(3)
20	TiO ₂ + TiO ₂ + M → (TiO ₂) ₂ + M	$1.4 \times 10^{-4} \exp(-48870/T)$ EQS ₂₀	(6)
21	(TiO ₂) ₃ + M → (TiO ₂) ₂ + TiO ₂ + M	$1.4 \times 10^{-9} \exp(-62411/T)$	(6)
22	(TiO ₂) ₂ + TiO ₂ + M → (TiO ₂) ₃ + M	$1.4 \times 10^{-9} \exp(-62411/T)$ EQS ₂₂	(6)
23	(TiO ₂) ₄ + M → (TiO ₂) ₃ + TiO ₂ + M	$1.4 \times 10^{-9} \exp(-53569/T)$	(6)
24	(TiO ₂) ₃ + TiO ₂ + M → (TiO ₂) ₄ + M	$1.4 \times 10^{-9} \exp(-53569/T)$ EQS ₂₄	(6)
25	(TiO ₂) ₄ + M → (TiO ₂) ₂ + (TiO ₂) ₂ + M	$1.4 \times 10^{-9} \exp(-57194/T)$	(6)
26	(TiO ₂) ₂ + (TiO ₂) ₂ + M → (TiO ₂) ₄ + M	$1.4 \times 10^{-9} \exp(-57914/T)$ EQS ₂₆	(6)
27	Si + OH → SiO + H	10^{-10}	(2)
28	Si + CO → SiO + C	$1.3 \times 10^{-9} \exp(-34513/T)$	(2)
29	Si + CO ₂ → SiO + CO	$2.72 \times 10^{-11} \exp(-282/T)$	(2)
30	Si + NO → SiO + N	$9 \times 10^{-11} (T/300)^{-0.96} \exp(-28/T)$	(2)
31	Si + O ₂ → SiO + O	$1.72 \times 10^{-10} (T/300)^{-0.53} \exp(-17/T)$	(2)
32	Si + O → SiO	$5.52 \times 10^{-18} (T/300)^{0.31}$	(2)
33	Si + OH → SiO + H	1×10^{-10}	(2)
34	SiO + OH → SiO ₂ + H	2×10^{-12}	(2)
35	SiO ₂ + H → SiO + OH	2×10^{-12} EQR ₅₁₆	(2)
36	Si + HCO ⁺ → SiH ⁺ + CO	1.6×10^{-9}	(2)
37	Si + P ⁺ → Si ⁺ + P	1×10^{-9}	(2)
38	Si + He ⁺ → Si ⁺ + He	3.3×10^{-9}	(2)
39	Si + S ⁺ → Si ⁺ + S	1.6×10^{-9}	(2)
40	Si ⁺ + OH → SiO ⁺ + H	$6.3 \times 10^{-10} (T/300)^{-0.5}$	(2)
41	Si ⁺ + H → Si + H	$1.17 \times 10^{-17} (T/300)^{-0.14}$	(2)
42	Si ⁺ + H ⁻ → Si + H	$7.51 \times 10^{-8} (T/300)^{-0.5}$	(2)
43	Si ⁺ + HF → SiF ⁺ + H	$5.7 \times 10^{-9} (T/300)^{-0.5}$	(2)
44	Si ⁺ + Na → Si + Na ⁺	2.7×10^{-9}	(2)
45	Si ⁺ + Fe → Si + Fe ⁺	1.9×10^{-9}	(2)
46	SiO ⁺ + N → Si ⁺ + NO	2.1×10^{-10}	(2)
47	SiO ⁺ + Fe → SiO + Fe ⁺	1×10^{-9}	(2)
48	SiO ⁺ + C → Si ⁺ + CO	1×10^{-9}	(2)
49	SiO ⁺ + O → Si ⁺ + O ₂	2×10^{-10}	(2)
50	SiO ₂ + He ⁺ → O ₂ + Si ⁺ + He	2×10^{-9}	(2)
51	SiH ⁺ + H → Si ⁺ + H ₂	1.9×10^{-9}	(2)
52	Si ⁺ + e ⁻ → Si + γ	$4.26 \times 10^{-12} (T/300)^{-0.61}$	(2)
53	SiO ⁺ + e ⁻ → Si + O	$2 \times 10^{-7} (T/300)^{-0.5}$	(2)
54	SiH ⁺ + e ⁻ → Si + H	$2 \times 10^{-7} (T/300)^{-0.5}$	(2)
55	SiF ⁺ + e ⁻ → Si + F	$2 \times 10^{-7} (T/300)^{-0.5}$	(2)

Notes. The first block describes the Ti chemistry; the second block describes the Si chemistry. For the definition of EQR_{*i*} see Boulangier et al. (2019), where *i* is the reaction number as defined in their work. References: (0) This work, (1) Campbell & McClean (1993), (2) McElroy et al. (2013), (3) Plane (2013), (4) Ritter & Weisshaar (2002), (5) Higuchi et al. (2008), (6) Kiefer et al. (2023).

Table E.2. Bulk growth reactions considered for this study. The list of reaction was taken from [Helling et al. \(2019\)](#). s_0 , s_1 , s_2 and s_3 are the fitting parameters of the vapor number density (Eq. 43). ΔV is the volume increase per bulk growth reaction.

nr	reaction	s_0	s_1 [K]	s_2 [K ²]	s_3 [K ³]	ΔV [cm ⁻³]
c1	Ti + 2 H ₂ O → TiO ₂ [s] + 2 H ₂	7.902e+01	-1.622e+05	-4.690e+06	9.013e+08	3.136e-23
c2	TiO ₂ → TiO ₂ [s]	6.194e+01	-6.731e+04	-5.024e+06	9.890e+08	3.136e-23
c3	TiO + H ₂ O → TiO ₂ [s] + H ₂	6.431e+01	-7.986e+04	-5.635e+06	1.084e+09	3.136e-23
c4	TiS + 2 H ₂ O → TiO ₂ [s] + H ₂ S + H ₂	5.244e+01	-2.031e+05	-4.500e+05	1.000e+00	3.136e-23
c5	2 Mg + SiO + 3 H ₂ O → Mg ₂ SiO ₄ [s] + 3 H ₂	1.695e+02	-2.951e+05	-1.166e+07	2.383e+09	7.278e-23
c6	2 MgOH + SiO + H ₂ O → Mg ₂ SiO ₄ [s] + 2 H ₂	1.429e+02	-1.986e+05	-1.275e+07	2.560e+09	7.278e-23
c7	2 Mg(OH) ₂ + SiO → Mg ₂ SiO ₄ [s] + H ₂ O + H ₂	8.983e+01	-3.337e+05	-4.754e+06	1.094e+09	7.278e-23
c8	2 MgH + SiO + 3 H ₂ O → Mg ₂ SiO ₄ [s] + 4 H ₂	1.591e+02	-2.695e+05	-1.247e+07	2.518e+09	7.278e-23
c9	2 Mg + SiS + 4 H ₂ O → Mg ₂ SiO ₄ [s] + H ₂ S + 3 H ₂	1.590e+02	-4.198e+05	-1.889e+06	1.000e+00	7.278e-23
c10	2 MgOH + SiS + 2 H ₂ O → Mg ₂ SiO ₄ [s] + H ₂ S + 2 H ₂	1.304e+02	-3.169e+05	-9.041e+06	1.909e+09	7.278e-23
c11	2 Mg(OH) ₂ + SiS → Mg ₂ SiO ₄ [s] + H ₂ + H ₂ S	8.892e+01	-3.312e+05	-5.254e+06	1.201e+09	7.278e-23
c12	2 MgH + SiS + 4 H ₂ O → Mg ₂ SiO ₄ [s] + H ₂ S + 4 H ₂	1.489e+02	-3.948e+05	-2.229e+06	1.000e+00	7.278e-23
c13	4 Mg + 2 SiH + 8 H ₂ O → 2 Mg ₂ SiO ₄ [s] + 9 H ₂	1.731e+02	-3.558e+05	-1.181e+07	2.406e+09	7.278e-23
c14	4 MgOH + 2 SiH + 4 H ₂ O → 2 Mg ₂ SiO ₄ [s] + 7 H ₂	1.466e+02	-2.594e+05	-1.290e+07	2.583e+09	7.278e-23
c15	4 Mg(OH) ₂ + 2 SiH → 2 Mg ₂ SiO ₄ [s] + 5 H ₂	1.051e+02	-2.737e+05	-9.116e+06	1.875e+09	7.278e-23
c16	4 MgH + 2 SiH + 8 H ₂ O → 2 Mg ₂ SiO ₄ [s] + 11 H ₂	1.628e+02	-3.303e+05	-1.262e+07	2.541e+09	7.278e-23
c17	SiO + H ₂ O → SiO ₂ [s] + H ₂	6.335e+01	-5.758e+04	-5.536e+06	1.075e+09	3.768e-23
c18	SiS + 2 H ₂ O → SiO ₂ [s] + H ₂ + H ₂ S	5.085e+01	-1.759e+05	-1.823e+06	4.249e+08	3.768e-23
c19	SiH + 2 H ₂ O → SiO ₂ [s] + 2 H ₂ + H	2.547e+01	-1.214e+05	-4.299e+06	8.301e+08	3.768e-23
c20	2 AlOH + H ₂ O → Al ₂ O ₃ [s] + 2 H ₂	8.592e+01	-1.837e+05	-2.900e+06	1.000e+00	4.265e-23
c21	2 AlH + 3 H ₂ O → Al ₂ O ₃ [s] + 4 H ₂	1.015e+02	-2.605e+05	-9.682e+06	2.040e+09	4.265e-23
c22	Al ₂ O + 2 H ₂ O → Al ₂ O ₃ [s] + 2 H ₂	8.493e+01	-1.698e+05	-9.002e+06	1.914e+09	4.265e-23
c23	2 AlO ₂ H → Al ₂ O ₃ [s] + H ₂ O	7.369e+01	-2.994e+05	-7.691e+05	1.000e+00	4.265e-23
c24	FeO → FeO[s]	5.784e+01	-5.214e+04	-5.698e+06	1.137e+09	1.992e-23
c25	Fe + H ₂ O → FeO[s] + H ₂	5.687e+01	-4.231e+04	-5.829e+06	1.140e+09	1.992e-23
c26	FeS + H ₂ O → FeO[s] + H ₂ S	5.660e+01	-3.904e+04	-6.238e+06	1.248e+09	1.992e-23
c27	Fe(OH) ₂ → FeO[s] + H ₂ O	2.854e+00	-2.023e+04	-1.184e+06	2.648e+08	1.992e-23
c28	2 FeH + 2 H ₂ O → 2 FeO[s] + 3 H ₂	4.592e+01	-2.430e+04	-5.662e+06	1.071e+09	1.992e-23
c29	FeS → FeS[s]	5.647e+01	-4.348e+04	-6.716e+06	1.289e+09	3.022e-23
c30	Fe + H ₂ S → FeS[s] + H ₂	5.673e+01	-4.675e+04	-6.307e+06	1.181e+09	3.022e-23
c31	FeO + H ₂ S → FeS[s] + H ₂ O	5.771e+01	-5.659e+04	-6.176e+06	1.177e+09	3.022e-23
c32	2 FeH + 2 H ₂ S → FeS[s] + 3 H ₂	4.579e+01	-2.874e+04	-6.140e+06	1.111e+09	3.022e-23
c33	2 Fe + 3 H ₂ O → Fe ₂ O ₃ [s] + 3 H ₂	1.097e+02	-2.119e+05	-9.578e+06	1.885e+09	5.032e-23
c34	2 FeO + H ₂ O → Fe ₂ O ₃ [s] + H ₂	9.543e+01	-1.597e+05	-1.067e+07	2.079e+09	5.032e-23
c35	2 Fe(OH) ₂ → Fe ₂ O ₃ [s] + H ₂ O + H ₂	2.885e+01	-2.487e+05	-1.944e+06	4.502e+08	5.032e-23
c36	2 FeS + 3 H ₂ O → Fe ₂ O ₃ [s] + 2 H ₂ S + H ₂	8.260e+01	-2.675e+05	-6.998e+06	1.433e+09	5.032e-23
c37	2 FeH + 3 H ₂ O → Fe ₂ O ₃ [s] + 4 H ₂	9.879e+01	-1.939e+05	-9.411e+06	1.816e+09	5.032e-23
c38	Mg + H ₂ O → MgO[s] + H ₂	5.870e+01	-5.209e+04	-4.378e+06	8.392e+08	1.869e-23
c39	2 MgOH → 2 MgO[s] + H ₂	2.061e+01	-7.653e+04	-1.259e+06	2.587e+08	1.869e-23
c40	Mg(OH) ₂ → MgO[s] + H ₂ O	5.951e+00	-3.197e+04	-4.611e+05	1.100e+08	1.869e-23
c41	2 MgH + 2 H ₂ O → 2 MgO[s] + 3 H ₂	4.839e+01	-2.657e+04	-5.190e+06	9.741e+08	1.869e-23
c42	SiO → SiO[s]	6.025e+01	-4.653e+04	-1.387e+06	2.685e+08	3.358e-23
c43	SiS + H ₂ O → SiO[s] + H ₂ S	5.935e+01	-4.397e+04	-1.887e+06	3.753e+08	3.358e-23
c44	2 SiH + 2 H ₂ O → 2 SiO[s] + 3 H ₂	4.865e+01	-4.527e+04	-2.760e+06	4.893e+08	3.358e-23
c45	2 Fe + SiO + 3 H ₂ O → Fe ₂ SiO ₄ [s] + 3 H ₂	1.679e+02	-2.708e+05	-1.494e+07	3.135e+09	7.708e-23
c46	2 Fe + SiS + 4 H ₂ O → Fe ₂ SiO ₄ [s] + H ₂ S + 3 H ₂	1.584e+02	-3.983e+05	-2.538e+06	1.000e+00	7.708e-23
c47	4 Fe + 2 SiH + 8 H ₂ O → 2 Fe ₂ SiO ₄ [s] + 9 H ₂	1.716e+02	-3.316e+05	-1.509e+07	3.158e+09	7.708e-23
c48	2 FeO + SiO + H ₂ O → Fe ₂ SiO ₄ [s] + H ₂	1.536e+02	-2.186e+05	-1.603e+07	3.329e+09	7.708e-23
c49	2 FeO + SiS + 2 H ₂ O → Fe ₂ SiO ₄ [s] + H ₂ S + H ₂	1.411e+02	-3.369e+05	-1.232e+07	2.678e+09	7.708e-23
c50	4 FeO + 2 SiH + 4 H ₂ O → 2 Fe ₂ SiO ₄ [s] + 5 H ₂	1.573e+02	-2.794e+05	-1.618e+07	3.352e+09	7.708e-23

Table E.2. continued.

nr	reaction	s_0	s_1 [K]	s_2 [K ²]	s_3 [K ³]	ΔV [cm ⁻³]
c51	$2 \text{FeS} + \text{SiO} + 3 \text{H}_2\text{O} \rightarrow \text{Fe}_2\text{SiO}_4[\text{s}] + 3 \text{H}_2\text{S}$	1.440e+02	-3.363e+05	-2.978e+06	1.000e+00	7.708e-23
c52	$2 \text{FeS} + \text{SiS} + 4 \text{H}_2\text{O}$ $\rightarrow \text{Fe}_2\text{SiO}_4[\text{s}] + 3 \text{H}_2\text{S} + \text{H}_2$	1.416e+02	-3.480e+05	-1.231e+07	2.678e+09	7.708e-23
c53	$4 \text{FeS} + 2 \text{SiH} + 8 \text{H}_2\text{O}$ $\rightarrow 2 \text{Fe}_2\text{SiO}_4[\text{s}] + 4 \text{H}_2\text{S} + 5 \text{H}_2$	1.477e+02	-3.972e+05	-3.045e+06	1.000e+00	7.708e-23
c54	$2 \text{Fe}(\text{OH})_2 + \text{SiO} \rightarrow \text{Fe}_2\text{SiO}_4[\text{s}] + \text{H}_2\text{O} + \text{H}_2$	8.704e+01	-3.075e+05	-7.303e+06	1.700e+09	7.708e-23
c55	$2 \text{Fe}(\text{OH})_2 + \text{SiS} \rightarrow \text{Fe}_2\text{SiO}_4[\text{s}] + \text{H}_2\text{S} + \text{H}_2$	8.614e+01	-3.049e+05	-7.803e+06	1.806e+09	7.708e-23
c56	$4 \text{Fe}(\text{OH})_2 + 2 \text{SiH} \rightarrow 2 \text{Fe}_2\text{SiO}_4[\text{s}] + 5 \text{H}_2$	1.023e+02	-2.474e+05	-1.167e+07	2.480e+09	7.708e-23
c57	$2 \text{FeH} + \text{SiO} + 3 \text{H}_2\text{O} \rightarrow \text{Fe}_2\text{SiO}_4[\text{s}] + 4 \text{H}_2$	1.570e+02	-2.528e+05	-1.477e+07	3.065e+09	7.708e-23
c58	$2 \text{FeH} + \text{SiS} + 4 \text{H}_2\text{O}$ $\rightarrow \text{Fe}_2\text{SiO}_4[\text{s}] + \text{H}_2\text{S} + 4 \text{H}_2$	1.474e+02	-3.801e+05	-2.614e+06	1.000e+00	7.708e-23
c59	$4 \text{FeH} + 2 \text{SiH} + 8 \text{H}_2\text{O}$ $\rightarrow 2 \text{Fe}_2\text{SiO}_4[\text{s}] + 11 \text{H}_2$	1.607e+02	-3.136e+05	-1.492e+07	3.089e+09	7.708e-23

Appendix F: Additional Plots

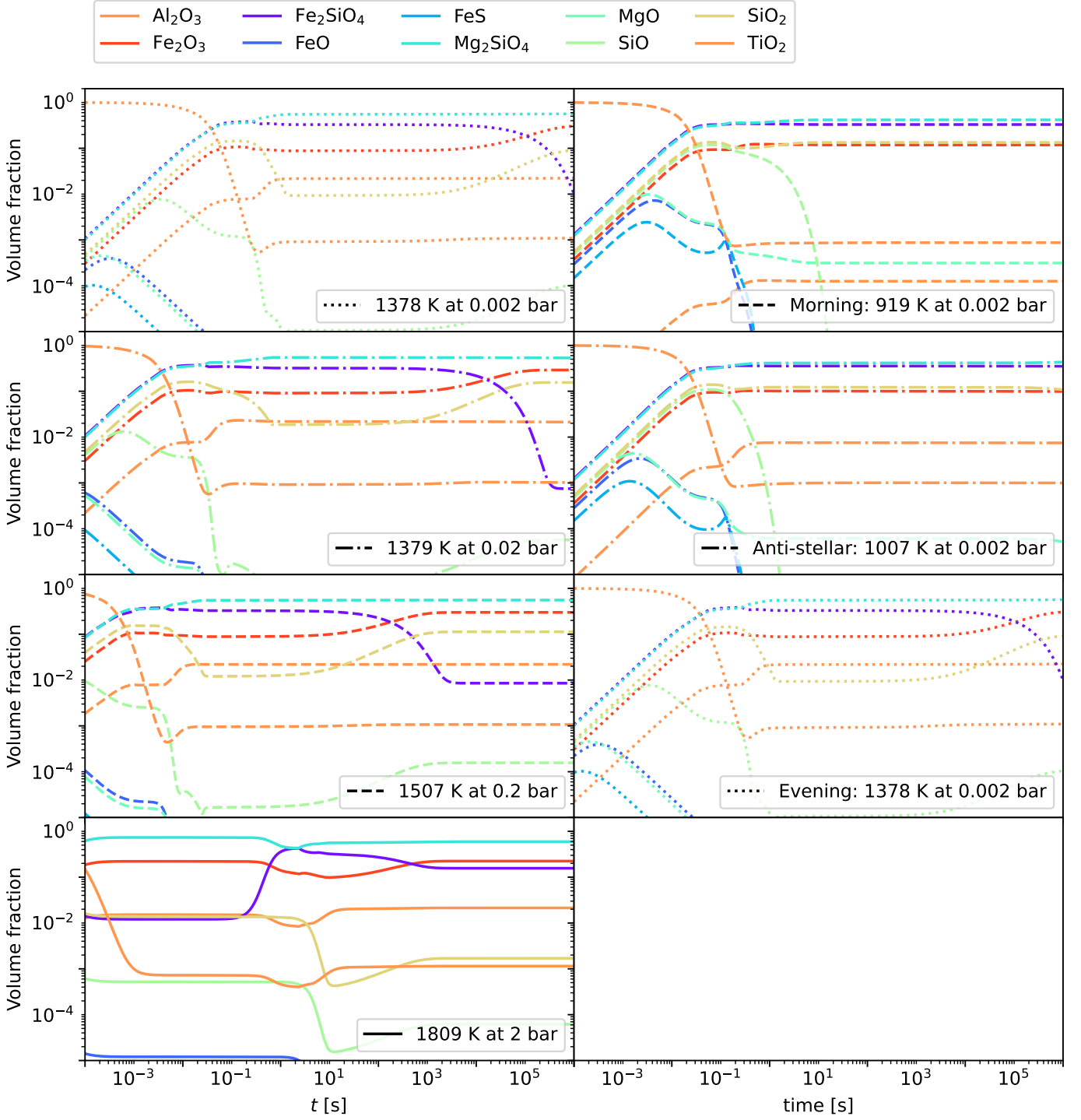


Fig. F.1. Volume fractions for the $T_{\text{gas}}-p_{\text{gas}}$ points of HD 209458 b. The sub-stellar point ($p_{\text{gas}} = 0.002$ bar, $T_{\text{gas}} = 2026$ K) is not shown since no cloud formation occurs.